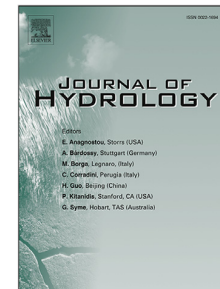


# Journal Pre-proof

Improvement of evapotranspiration simulation in a physically based ecohydrological model for the groundwater-soil-plant-atmosphere continuum

Kun Zhang, Gaofeng Zhu, Ning Ma, Huiling Chen, Shasha Shang



PII: S0022-1694(22)01010-1

DOI: <https://doi.org/10.1016/j.jhydrol.2022.128440>

Reference: HYDROL 128440

To appear in: *Journal of Hydrology*

Received date: 11 June 2022

Revised date: 4 August 2022

Accepted date: 25 August 2022

Please cite this article as: K. Zhang, G. Zhu, N. Ma et al., Improvement of evapotranspiration simulation in a physically based ecohydrological model for the groundwater-soil-plant-atmosphere continuum. *Journal of Hydrology* (2022), doi: <https://doi.org/10.1016/j.jhydrol.2022.128440>.

This is a PDF file of an article that has undergone enhancements after acceptance, such as the addition of a cover page and metadata, and formatting for readability, but it is not yet the definitive version of record. This version will undergo additional copyediting, typesetting and review before it is published in its final form, but we are providing this version to give early visibility of the article. Please note that, during the production process, errors may be discovered which could affect the content, and all legal disclaimers that apply to the journal pertain.

© 2022 Elsevier B.V. All rights reserved.

# Improvement of evapotranspiration simulation in a physically based ecohydrological model for the groundwater-soil-plant-atmosphere continuum

Kun Zhang<sup>a,e,\*</sup>, Gaofeng Zhu<sup>b,\*</sup>, Ning Ma<sup>c</sup>, Huiling Chen<sup>b</sup>, Shasha Shang<sup>d</sup>

<sup>a</sup>*Department of Mathematics, The University of Hong Kong, Hong Kong, China*

<sup>b</sup>*College of Earth and Environmental Sciences, Lanzhou University, Lanzhou, China*

<sup>c</sup>*Key Laboratory of Water Cycle and Related Land Surface Processes, Institute of Geographic Sciences and Natural Resources Research, Chinese Academy of Sciences, Beijing, China*

<sup>d</sup>*Tianjin Key Laboratory of Water Resources and Environment, Tianjin Normal University, Tianjin, China*

<sup>e</sup>*School of Biological Sciences, The University of Hong Kong, Hong Kong, China*

## Abstract

Accurate quantification of terrestrial evapotranspiration (ET) is essential to understanding the interaction between land and atmosphere, as well as the feedback response of vegetation dynamics. In our previous work, a physically based ecohydrological model called the simple terrestrial hydrophere (SiTH) model was developed to estimate ET and the other ET-related variables based on the groundwater-soil-plant-atmosphere continuum (GSPAC). However, the SiTH model (SiTHv1) still has some deficiencies in the model structure and parameters, which can result in potential uncertainty in the estimation of terrestrial ET. In this study, we aimed to address these limitations by developing a new version of the SiTH model (SiTHv2). The main modifications of the SiTHv2 model include: 1) the vegetation moisture constraint module is updated with vegetation optical depth observations; 2) the critical model parameters associated with root distribution are constrained using flux observations; 3) the soil module is extended to a three-layer module with 5 m of total depth; 4) an irrigation input water strategy is applied in the cropland areas; and 5) the latest ERA5-Land reanalysis data with a finer spatial resolution are used as the meteorological forcing data. The estimated ET of the SiTHv2 model was validated/compared at multiple scales (i.e., site/plot, basin, and global) with flux data, basin water balance data, and other mainstream global ET products, respectively. The results demonstrate that the SiTHv2 model performs better than the SiTHv1 model, with an improvement in the overall model root-mean-square error of 0.66 mm

day<sup>-1</sup> (plot scale) and 98.58 mm year<sup>-1</sup> (basin scale), representing 27% and 22% improvements over the SiTHv1 model in the same circumstances, respectively. In addition, the performance of the SiTHv2 model ranks well when compared to the existing terrestrial ET models and products. The improvements to the SiTH model should allow improved estimation of terrestrial ET and provide support to potential studies in water transfer within the GSPAC.

*Keywords:* Evapotranspiration, Water stress, SiTH model, Multi-scale verification

## 1 1. Introduction

2 Terrestrial evapotranspiration (ET) is a crucial nexus that is tightly coupled with the global wa-  
 3 ter cycle and energy balance (Oki and Kanae, 2006). About 65% of land precipitation is supplied  
 4 by the terrestrial ET process (Ma et al., 2021; Dorigo et al., 2021), which concomitantly consumes  
 5 more than 50% of the net solar radiation received by the land surface (Trenberth et al., 2009). In  
 6 recent decades, much effort has been devoted to estimating large-scale terrestrial ET using ecohy-  
 7 drological models and remote sensing technology (Fisher et al., 2008; Jung et al., 2019; Ma et al.,  
 8 2019; Martens et al., 2017; Mu et al., 2011). Accurate estimation of terrestrial ET fluxes is a key  
 9 goal of the ecohydrological community and benefits many scientific fields and practical applica-  
 10 tions, such as studies of the water/carbon cycle under the scenario of climate change (Frankenberg  
 11 et al., 2011; Held and Soden, 2006; Ma and Zhang, 2022; Zhou et al., 2021), the detection of  
 12 extreme events (Miralles et al., 2019; Teuling et al., 2010), and agricultural water management  
 13 (Allen et al., 2011; Xu et al., 2020).

14 Despite the sustained advances in global ET modeling that have been achieved over the past  
 15 few decades (Ma et al., 2021; Pan et al., 2020; Wang and Dickinson, 2012; Zhang et al., 2016),  
 16 there is still a need to characterize the ET processes in a more realistic and detailed manner, thereby  
 17 improving ET estimation overall. Among the different models, the simple terrestrial hydrosphere  
 18 (SiTH) model (Zhu et al., 2019) was proposed to simulate the terrestrial ET process within the con-  
 19 text of the groundwater-soil-plant-atmosphere continuum (GSPAC) (Scanlon and Kustas, 2012).

\*Corresponding author: kunzh@hku.hk (K.Z.) and zhugf@lzu.edu.cn (G.Z.)

20 In brief, the SiTH model depicts an integrated water path between vegetation canopy and ground-  
21 water, and is one of the few global ET models that considers the effect of groundwater in the root  
22 zone in regulating soil moisture conditions ([Fan, 2015](#)), which can mitigate the impact of drought  
23 in areas with a shallow groundwater depth ([Gou and Miller, 2014](#)). Another significant feature in  
24 the SiTH model is the ability to adjust the allocation of potential plant transpiration to different soil  
25 layers, combined with root distribution and soil water conditions. [Chen et al. \(2022\)](#) reported that  
26 the SiTH model performed well compared to other process-based global ET models for estimating  
27 the different ET components, such as soil evaporation, plant transpiration, and canopy intercepted  
28 evaporation, across various plant functional types (PFTs).

29 Nevertheless, there are still some limitations to the SiTH model. Firstly, the previous SiTH  
30 model (SiTHv1) did not take the plant moisture status into account, which can lead to poten-  
31 tial over-estimation when estimating ET, due to the weak moisture constraint, especially in forest  
32 ecosystems ([Chen et al., 2020](#)). Fortunately, microwave-based remote sensing technology has the  
33 capacity to monitor plant water content via the indicator of vegetation optical depth (VOD), which  
34 is based on the attenuation of passive and active microwave observations yielded by vegetation  
35 ([Jackson and Schmugge, 1991; Moesinger et al., 2020; Owe et al., 2008](#)). In this present study, we  
36 attempted to incorporate VOD into the SiTH model, in order to better characterize water stress for  
37 vegetation growth. Secondly, the SiTHv1 model regards precipitation to be the only source of in-  
38 put water applied to cropland. However, around 40% of the global cropland is made up of irrigated  
39 land, which contributes 60% of the global food supply and concurrently consumes approximately  
40 70% of the global freshwater withdrawal from the surface/subsurface water system ([Foley et al.,](#)  
41 [2011; Siebert and Döll, 2010](#)). Thus, an irrigation water use (IWU) scheme is introduced in the  
42 updated SiTH model, based on the authors' prior work on satellite-based global IWU estimation  
43 ([Zhang et al., 2022](#)). Thirdly, plant transpiration generally dominates the total ET ([Jasechko et al.,](#)  
44 [2013](#)), and is typically governed by the soil water availability and the root distribution, which are  
45 given as empirical parameters in the SiTHv1 model. Hence, in the updated SiTH model, the soil  
46 module is changed to three layers, and the total depth is extended to 5 m, allowing the model to  
47 cover the majority of the global root depths for the various PFTs ([Canadell et al., 1996; Maeght](#)  
48 [et al., 2013](#)). In addition, the fundamental parameters related to plant root distribution are op-

49 timized using global flux observations. Lastly, the meteorological forcing data are replaced by  
 50 the fifth generation of European reanalysis data (ERA5-Land, hereafter referred to as ERA5L) to  
 51 run this updated SiTH model at a global scale. The ERA5L product is a state-of-the-art reanaly-  
 52 sis product developed by the European Centre for Medium-Range Weather Forecasts (ECMWF),  
 53 which offers spatio-temporally continuous data at a finer spatial resolution ( $0.1^\circ$  globally).

54 The focus of this study was to present an updated version of the SiTH model (SiTHv2), which  
 55 includes: 1) modification of the model structure with new features; 2) multi-scale validation of the  
 56 SiTHv2 model using eddy covariance flux measurements and basin-scale water balance estimates;  
 57 and 3) a global comparison of the SiTH-based ET estimates with other mainstream global ET  
 58 products, in terms of magnitude and trend changes. In addition, we produced a global daily ET  
 59 dataset with a spatial resolution of  $0.1^\circ$ , based on the newly modified SiTHv2 model.

## 60 2. Methods

### 61 2.1. Model development

62 In the previous version (Zhu et al., 2019), the SiTH model was proposed for continuous mod-  
 63 eling of the water path in the GSPAC (Fig. 1). The total ET estimated from the SiTH model is the  
 64 sum of the bare soil evaporation ( $E_s$ ), plant transpiration ( $T_r$ ), and canopy intercepted evaporation  
 65 ( $E_i$ ). It is worth noting that the water stress on  $E_s$  is constrained by the first soil layer, while  $T_r$  is  
 66 constrained by both the multiple soil layers and the groundwater (if the groundwater can recharge  
 67 to the root zone).

$$ET = E_i + E_s + T_r \quad (1)$$

$$E_i = f_{\text{wet}} \cdot \alpha \cdot \frac{\Delta}{\Delta + \gamma} \cdot \frac{R_{\text{nc}}}{\lambda} \quad (2)$$

$$E_s = f_{\text{sm}} \cdot \alpha \cdot \frac{\Delta}{\Delta + \gamma} \cdot \frac{R_{\text{ns}} - G}{\lambda} \quad (3)$$

$$T_r = (1 - f_{\text{wet}}) \cdot f_v \cdot f_t \cdot \left[ \sum_{i=1}^n (f_{\text{smv},i} \cdot T_{\text{ps},i}) + \sum_{i=1}^n (T_{\text{pg},i}) \right] \quad (4)$$

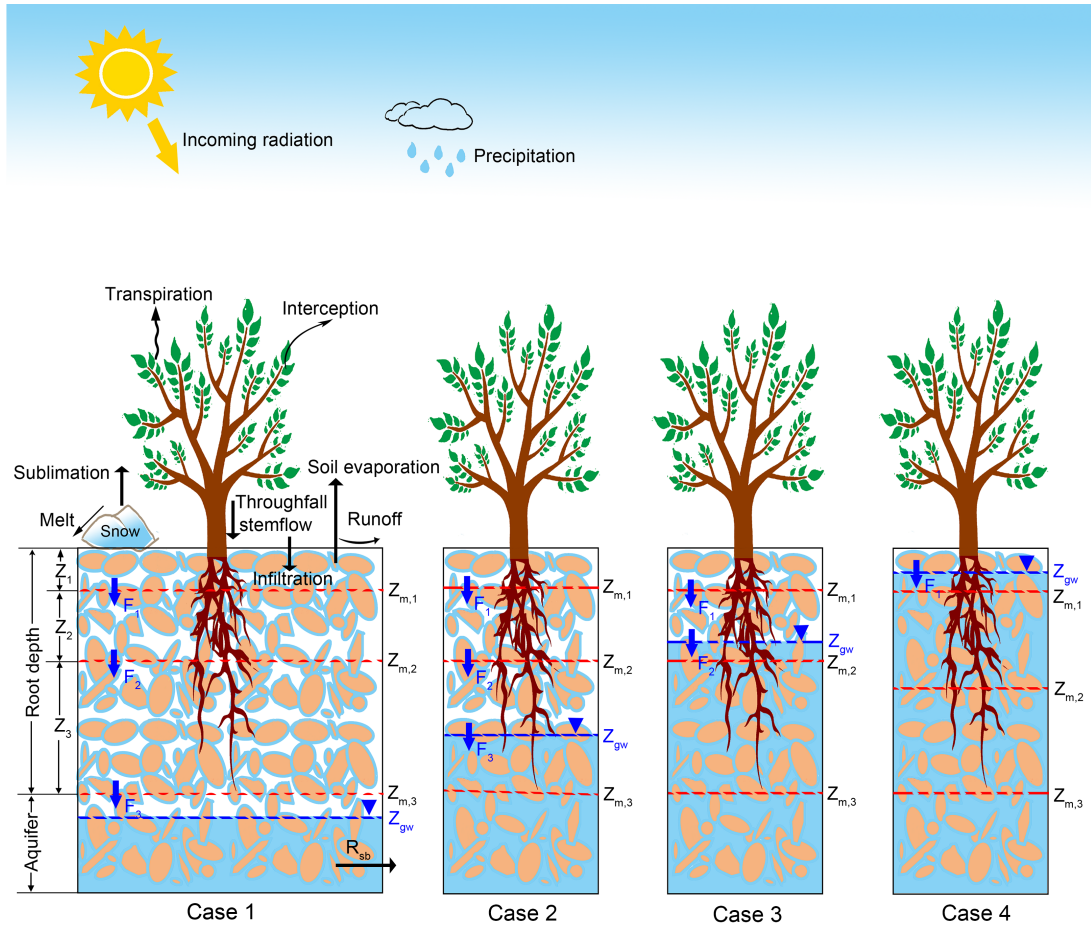


**Fig. 1.** Schematic representation of the hydrologic process in the SiTH model. Case 1 represents the groundwater table being below the root zone; Case 2 represents the groundwater table being within the third soil layer; Case 3 and Case 4 represent the groundwater table being within the second and first soil layer, respectively. The arrows indicate the water flux direction.

where  $\alpha$  is the Priestly-Taylor coefficient, which is set to 1.26;  $\Delta$  is the slope of the saturated vapor pressure curve ( $\text{kPa } ^\circ\text{C}^{-1}$ ;  $\gamma$  is the psychrometric constant, which is set to 0.066 ( $\text{kPa } ^\circ\text{C}^{-1}$ );  $\lambda$  is the latent heat of evaporation ( $\text{MJ kg}^{-1}$ );  $G$  is the soil heat flux ( $\text{W m}^{-2}$ ); and  $n$  is the total number of soil layers ( $n = 3$ ) in the SiTHv2 model.  $R_{ns}$  and  $R_{nc}$  are the net radiation ( $R_n$ ) allocated to the bare soil and canopy surface ( $\text{W m}^{-2}$ ), respectively, which are complementary ( $R_n = R_{nc} + R_{ns}$ ). Their calculation is conducted according to  $R_{ns} = R_n \exp(-k_{R_n} \text{LAI})$  (Beer, 1852; Fisher et al., 2008), where  $k_{R_n}$  is the extinction coefficient, which is set to 0.6 (Impens and Lemeur, 1969).  $T_{ps,i}$  and  $T_{pg,i}$  are the potential transpiration from the unsaturated  $i$ th layer and saturated  $i$ th layer, which can

76 be derived from the total potential ET by considering the vertical distributions of plant roots and the  
 77 depth of the groundwater table (see details in [Zhu et al. \(2019\)](#)). The  $f$ -functions are the different  
 78 constraints on the potential evaporation and transpiration, where  $f_{\text{wet}}$  is the relative surface wetness,  
 79  $f_v$  is the vegetation water stress on the plant transpiration,  $f_{\text{sm}}$  is the soil moisture constraint on the  
 80 bare soil evaporation,  $f_{\text{smv},i}$  is the soil moisture constraint on the plant transpiration at the  $i$ th soil  
 81 layer, and  $f_t$  is the temperature constraint on plant growth. Among the different constraints,  $f_{\text{wet}}$ ,  
 82  $f_t$ , and  $f_{\text{sm}}$  can be calculated as:

$$f_{\text{wet}} = \min \left\{ \chi \cdot \frac{S_c}{T_p}, 1 \right\} \quad (5)$$

$$f_t = \exp \left[ - \left( \frac{T_a - T_{\text{opt}}}{T_{\text{opt}}} \right)^2 \right] \quad (6)$$

$$f_{\text{sm}} = \begin{cases} 0, & \text{if } \theta_i \leq \theta_{\text{wp}} \\ \frac{\theta_i - \theta_{\text{wp}}}{\theta_{\text{fc}} - \theta_{\text{wp}}}, & \text{if } \theta_{\text{wp}} < \theta_i < \theta_{\text{fc}} \\ 1, & \text{if } \theta_i \geq \theta_{\text{fc}} \end{cases} \quad (7)$$

83 where  $T_p$  is the potential transpiration rate of the canopy;  $\chi$  is the fractional interception occurring  
 84 during daytime, which is set to 0.7;  $S_c$  is the water storage capacity of the canopy, which is defined  
 85 as the product of precipitation and the leaf area index (LAI);  $T_a$  is the air temperature ( $^{\circ}\text{C}$ );  $T_{\text{opt}}$  is  
 86 the optimum plant growth temperature ( $^{\circ}\text{C}$ ), which can be defined as the air temperature when the  
 87 product of LAI,  $R_n$ , and  $T_a$  is the highest during the growing season;  $\theta_{\text{fc}}$  is the soil field capacity;  
 88  $\theta_{\text{wp}}$  is the soil moisture at the wilting point; and  $\theta_i$  is the actual soil moisture at the  $i$ th soil layer  
 89 (the first soil layer is only considered for the soil evaporation).

90 Notably, the critical threshold ( $\theta_c$ ) for soil moisture in the SiTH model is the multifactor-  
 91 influenced parameter representing the state at which soil moisture begins to have a constraint on  
 92 plant transpiration, which dominates the transpiration changes in transitional regimes ([Schwing-](#)  
 93 [shackl et al., 2017; Wang et al., 2022](#)). Instead of only considering the soil type as a static constant,  
 94 as in the SiTHv1 model, we revised the expression of ( $\theta_c$ ) in the SiTHv2 model to reflect the char-

95 characteristic water stress sensitivities for different PFTs, according to Purdy et al. (2018) and van  
 96 Diepen et al. (1989):

$$\theta_c = (1 - p)(\theta_{fc} - \theta_{wp}^h) + \theta_{wp}^h \quad (8)$$

$$p = \frac{1}{1 + ET_p} - \frac{b}{1 + H_c} \quad (9)$$

$$\theta_{wp}^h = \theta_{wp}/k \quad (10)$$

97 where  $k$  is a sensitivity index for the soil water content, which can be determined as the square root  
 98 of the canopy height ( $H_c$ );  $\theta_{wp}^h$  is the adjusted wilting point for soil moisture when considering  $H_c$ ;  
 99  $p$  is a parameter for regulating  $\theta_c$  between  $\theta_{fc}$  and  $\theta_{wp}^h$ , which can be determined by the potential  
 100 ET ( $ET_p$ ) and  $H_c$ ; and  $b$  denotes the weight of  $H_c$  on  $\theta_c$ , which is set to 0.1. Thus, the soil  
 101 moisture constraint function for plant transpiration at the  $i$ th layer ( $f_{smv,i}$ ) can be expressed as  
 102 follows (Martens et al., 2017):

$$f_{smv,i} = \begin{cases} 0, & \text{if } \theta_i \leq \theta_{wp}^h \\ 1 - \left( \frac{\theta_c - \theta_i}{\theta_c - \theta_{wp}^h} \right)^k, & \text{if } \theta_{wp}^h \leq \theta_i \leq \theta_c \\ 1, & \text{if } \theta_i \geq \theta_c \end{cases} \quad (11)$$

103 Fig. 2 illustrates a concept map of the response of  $f_{smv}$  to the gradients of soil water content  
 104 under different biotic and abiotic conditions (i.e.,  $H_c$  and  $ET_p$ ). Clearly, the soil water constraint  
 105 scheme for transpiration adopted by the SiTHv1 model (yellow line) is simplified as a logarithmic  
 106 function to soil water content, where  $f_{smv}$  decreases rapidly from the critical point of soil moisture.  
 107 However, the new constraint scheme in the SiTHv2 model provides a wide range of  $f_{smv}$  to a  
 108 specific value of  $\theta$ , based on different  $H_c$  and  $ET_p$  values, which is more in line with the real  
 109 situation of vegetation (e.g., forest or grassland), where the sensitivity to soil moisture varies over  
 110 different plant heights with specific environmental conditions.

111 Furthermore, the plant transpiration estimated by the SiTHv1 model is not constrained by the

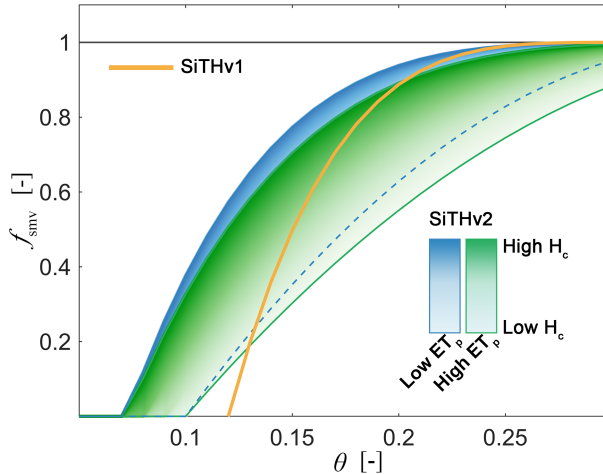


**Fig. 2.** Schematic diagram of the soil water constraint on transpiration in SiTHv2 by considering the different vegetation height and environmental conditions.

moisture content of the vegetation status. To address this issue, we added a plant water stress module based on the microwave remotely sensed VOD. It has been well documented that VOD is closely related to the density, type, and water content of vegetation, and is advantageous for monitoring tropical forest without the effect of cloud (Liu et al., 2011, 2015). In the SiTHv2 model, the vegetation water stress ( $f_v$ ) is described as follows:

$$f_v = \sqrt{\frac{VOD}{VOD_{max}}} \quad (12)$$

where  $VOD_{max}$  is the maximum value for the annual VOD time series at each pixel.

In addition, to better estimate the ET from irrigated cropland, we introduced an IWU scheme into the SiTHv2 model. The irrigation signal can be first identified by the discrepancy between the dynamic changes of soil moisture and precipitation in the irrigated area. The volume of the IWU can then be derived based on the balanced relationship of the soil water variations (Zhang et al., 2022). The IWU estimates were obtained from the authors' prior work, and were integrated into the SiTH model as exceptional input water applied to the cropland. Specifically, the original monthly IWU estimates for global irrigated land were simply dispersed to the start, the middle, and the end of a month by weighting of the distribution density of the LAI. This can be expected to enhance the water supply in the irrigated regions during the growing season, especially at a

127 long-term time scale (i.e., monthly or yearly).

128 *2.2. Parameter optimization scheme*

129 In the SiTHv2 model, the soil layer is extended to a total depth of 5 m, to better accommodate  
 130 the root zone of forest. Thus, we re-optimized two critical parameters, D50 and D95, which are  
 131 fundamental for representing at least 50% or 95% of the root system above the depth of D50  
 132 or D95, respectively. Based on the observed ET at each eddy covariance (EC) flux station, we  
 133 used the differential-evolution Markov chain (DE-MC) algorithm (Ter Braak and Vrugt, 2008) to  
 134 obtain the posterior distribution of D50 and D95 globally. In general, the posterior distribution of  
 135 the candidate parameter sets ( $\phi$ ) in a Bayesian framework can be expressed as:

$$f(\phi | ET_{obs}) = f(\phi) \prod_{t=1}^T \frac{1}{\sqrt{2\pi}\sigma^2} \exp\left(-\frac{(ET_{sim}(\phi; t) - ET_{obs}(t))^2}{2\sigma^2}\right) \quad (13)$$

136 where  $f(\phi)$  represents the prior parameter distributions;  $f(\phi | ET_{obs})$  represents the posterior pa-  
 137 rameter distributions;  $t$  is the time step (i.e., days);  $T$  is the total number of observations/simulations;  
 138  $ET_{obs}$  is the observed ET data at the flux station;  $ET_{sim}$  is the simulated ET from the SiTHv2 model;  
 139 and  $\sigma$  is the standard deviation of the model error. In the DE-MC algorithm, the parameter pro-  
 140 posals ( $\phi_p$ ) are generated based on two randomly selected chains ( $\phi_{r1}$  and  $\phi_{r2}$ ), and the difference  
 141 is multiplied by a scaling factor ( $\rho$ ) and added to the current chain ( $\phi_i$ ):

$$\phi_p = \phi_i + \rho (\phi_{r1} - \phi_{r2}) + e \quad (14)$$

142 where the scaling factor  $\rho$  can be set to  $2.38\sqrt{2d}$ , and  $d$  is the dimension of parameter sets; and  
 143  $e$  is selected from a symmetrical distribution and represents a probabilistic acceptance rule in the  
 144 DE-MC algorithm.

145 Specifically, in this study, we performed 12 chains in parallel with a total of 10000 iterations,  
 146 including a burn-in time of 500 iterations. During the optimization, five-fold cross-validation was  
 147 utilized in the parameter optimization approach. The flux data were divided into five subsamples,  
 148 with one subsample preserved as the data for validating the model, while the remaining four sub-  
 149 samples were used as the target function. This cross-validation procedure was repeated five times,

150 and the results were then averaged to obtain an optimal solution for each site. This strategy maxi-  
 151 mizes the data utilization and can mitigate the overfitting and selection bias in the optimization. In  
 152 addition, we employed a double-optimization scheme to implement parameter optimization at the  
 153 PFT scale. This means that the optimal solutions for each site were first optimized using the site-  
 154 observed ET as the target, to achieve the best root-mean-square error at the site level (S-RMSE).  
 155 The optimal parameters for the individual PFTs could then be determined based on the posterior  
 156 distribution of the parameters closest to the obtained S-RMSE for a particular PFT (Zhang et al.,  
 157 2019a). This procedure ensured that the optimized parameters were optimally balanced in each  
 158 PFT-specific site, even though the length of the valid data varied from site to site. The estimated  
 159 posterior distribution of D50 and D95 for the different PFTs are given in Appendix (Fig. A1).

160 2.3. *Model performance evaluation metrics*

161 To ensure that the ET-related variables can reach equilibrium, a 50-year spin-up was carried  
 162 out by repeating the forcing from 2001 to 2005 10 times. The model was then run at the end of  
 163 the spin-up to generate the global ET estimates. We also employed several statistical metrics to  
 164 quantify the model performance in this study. Among the different metrics, a Taylor diagram was  
 165 used to show the differences between the SiTHv2 and SiTHv1 models across multiple flux sites  
 166 and PFTs. In a Taylor diagram, the model performance can be characterized as a comprehensive  
 167 indicator, the Taylor skill score (TS-score), which is based on the correlation coefficient ( $R$ ) and  
 168 the normalized standard deviation (Zhang et al., 2017). Thus, each point in a Taylor diagram can  
 169 be scored as:

$$S = \frac{2(1 + R)}{[(\sigma_s/\sigma_o) + 1 / (\sigma_s/\sigma_o)]^2} \quad (15)$$

170 where  $S$  is the TS-score bounded by zero and unity, where unity represents perfect agreement  
 171 with the observation; and  $\sigma_s$  and  $\sigma_o$  are the standard deviations of the simulation and observation,  
 172 respectively. The root-mean-square error (RMSE) and the Nash-Sutcliffe efficiency coefficient  
 173 (NSE) were also included in the statistical analysis for the comparison of the various ET mod-  
 174 els/products. These metrics are calculated as follows:

$$\text{RMSE} = \sqrt{\frac{1}{T} \sum_{t=1}^T [O(t) - M(t)]^2} \quad (16)$$

$$\text{NSE} = 1 - \frac{\sum_{t=1}^T [O(t) - M(t)]^2}{\sum_{t=1}^T [O(t) - \bar{O}]^2} \quad (17)$$

175 where  $O(t)$  and  $M(t)$  are the observed and simulated data at time  $t$ , respectively; and  $\bar{O}$  is the mean  
 176 value of the observed data. In general, the better the model performance, the lower the value of  
 177 the RMSE and the closer the NSE value is to 1.

### 178 3. Data

#### 179 3.1. Eddy covariance data

180 We used the observed meteorological and flux data from 175 EC stations globally (see Table  
 181 S1 in the Supplementary information) to optimize the candidate parameters and evaluate model  
 182 performance at the plot scale. These data were obtained from the FLUXNET2015 dataset ([Pa-](#)  
 183 [storello et al., 2020](#)) and contain 12 kinds of major PFTs under different climate zones ([Fig. 3](#)).  
 184 It should be noted that quality control of the flux data is necessary before using these data in the  
 185 parameter optimization procedure. The flux data (half-hourly) were considered missing in this  
 186 study if the energy balance residual term (i.e., the net radiation minus the sum of the latent heat,  
 187 sensible heat, and geothermal heat) exceeded  $300 \text{ W m}^{-2}$ . Linear interpolation was performed on  
 188 the missing data if the data gap was less than 6 hours in a day. After the pre-processing step,  
 189 the quality of the EC data used in this study was strictly corrected, which ensured that the energy  
 190 closure was generally above 70% at all the different PFTs. Finally, the flux data for each selected  
 191 EC station were processed to a daily time series.

#### 192 3.2. Inputs of the SiTHv2 model for global application

##### 193 3.2.1. Remote sensing data

194 The dynamics of land vegetation are important to determine the energy partitioning when esti-  
 195 mating terrestrial ET. To characterize the variation of vegetation growth, the LAI dataset (Version

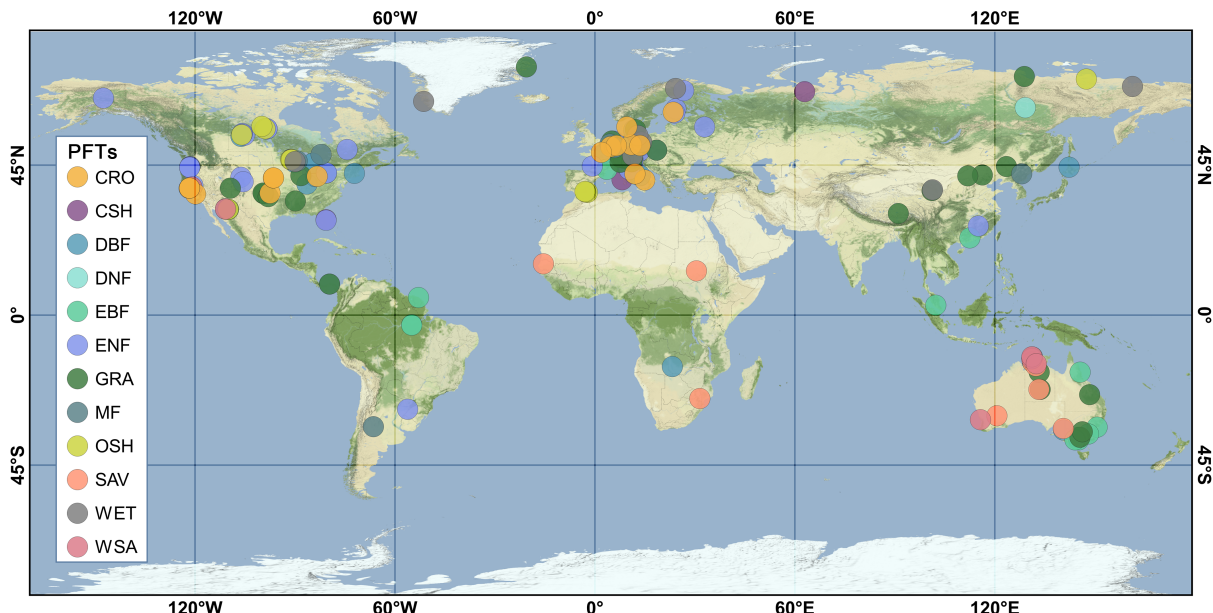


**Fig. 3.** Global distribution of the EC stations used in this study. The PFTs are according to the International Geosphere-Biosphere Programme (IGBP) ecosystem surface classification system. CRO: croplands; CSH: closed shrublands; DBF: deciduous broadleaf forest; DNF: deciduous needleleaf forest; EBF: evergreen broadleaf forest; ENF: evergreen needleleaf forest; GRA: grasslands; MF: mixed forest; OSH: open shrublands; SAV: savannas; WET: wetland; WSA: woody savannas.

196 50) from the Global Land Surface Satellite (GLASS) product (Liang et al., 2021) was used in this  
 197 study. This LAI dataset was initially developed from Moderate Resolution Imaging Spectroradiometer (MODIS) data with a spatial resolution of  $0.05^{\circ}$  for the period of 2001–2018. Further-  
 198 more, to depict the vegetation water content in the SiTHv2 model, we used a VOD product from  
 199 the VOD Climate Archive (VODCA), which is based on microwave observations from multiple  
 200 sensors and can be divided into different spectral bands (Moesinger et al., 2020). The  $0.25^{\circ}$  daily  
 201 X-band VODCA product with a continuous coverage from 2001 to 2018 was used in this study.  
 202

203 The land surface net radiation data used in this study were derived from the Clouds and the  
 204 Earth's Radiant Energy System (CERES) project, which provides satellite-based observations of  
 205 the Earth's radiation budget (Kato et al., 2018). Specifically, we selected the synoptic top of atmo-  
 206 sphere (TOA) and surface fluxes and clouds (SYN) product and calculated the net surface radiation  
 207 from the Level 3 SYN1deg dataset with the up/down shortwave/longwave flux. In addition, the

208 global dynamic PFT distribution was obtained from the MODIS land-cover product (MCD12C1)  
 209 with a spatial resolution of 0.05° globally ([Sulla-Menashe et al., 2019](#)). The main types of PFTs in  
 210 the MCD12C1 product are in accordance with the International Geosphere-Biosphere Programme  
 211 (IGBP) land-cover classification system. The details of the selected remote sensing data are sum-  
 212 marized in [Table 1](#).

**Table 1.** Summary of selected remote sensing products in current study.

Variable	Product	Version	Spatial resolution	Period <sup>(1)</sup>	Reference
LAI	GLASS	V50	0.05°	2001–2018	<a href="#">Liang et al. (2021)</a>
VOD	VODCA	X-Band	0.25°	2001–2018	<a href="#">Moesinger et al. (2020)</a>
Radiation	CERES	SYN1deg(L3)	1°	2001–2018	<a href="#">Kato et al. (2018)</a>
Landcover	MODIS	MCD12C1	0.05°	2001–2018	<a href="#">Sulla-Menashe et al. (2019)</a>

Note: (1) the time span shown here indicates the period used in the current study.

### 213 3.2.2. Meteorological and ancillary data

214 The meteorological variables in the SiTHv2 model, including the 2-m air temperature ( $T_a$ ),  
 215 surface air pressure ( $P_a$ ), and the total precipitation ( $P_{tot}$ ), were obtained from the ERA5L product  
 216 ([Muñoz-Sabater et al., 2021](#)) produced by the ECMWF at a spatial resolution of 0.1°. The original  
 217 half-hourly ERA5L product was selected in this study, followed by aggregation to a daily scale to  
 218 match the temporal interval in the SiTHv2 model. The global soil type map used in the SiTHv2  
 219 model was derived from the Harmonized World Soil Database (HWSD) v1.2 ([Wieder et al., 2014](#)),  
 220 which combines the available soil information from regional and national institutes worldwide and  
 221 provides a soil raster database with a 30 arc-second resolution.

### 222 3.3. Water balance based evapotranspiration data

223 In addition to evaluating the estimates of terrestrial ET at selected flux sites, we also used  
 224 independent ET estimates to test the SiTHv2 model at a basin scale. The water-balanced evapo-  
 225 transpiration estimates ( $ET_{wb}$ ) were generated from the residual of the water balance equation:

$$ET_{wb} = P - R - \Delta S \quad (18)$$

226 where  $P$  is the annual precipitation ( $\text{mm year}^{-1}$ );  $R$  is annual runoff for each basin; and  $\Delta S$  is  
 227 the changes in terrestrial water storage. A total of 49 basins from [Ma et al. \(2021\)](#) were selected,  
 228 which represent a broad range of climate zones and PFTs. The precipitation data were acquired  
 229 from the Global Precipitation Climatology Center (GPCC) Full Data Monthly Product Version  
 230 2018 ([Schneider et al., 2018](#)) for most basins, while the Parameter-elevation Regressions on In-  
 231 dependent Slopes Model (PRISM) precipitation data ([Daly et al., 2008](#)) were used for basins in  
 232 the continental United States because the PRISM product is considered to be the most accurate  
 233 precipitation product for the United States ([Lundquist et al., 2015](#)). The measured runoff data for  
 234 these basins were obtained from the Global Runoff Data Center, the China Sediment Bulletin, and  
 235 the United States Geological Survey. The  $\Delta S$  was extracted from the Gravity Recovery and Cli-  
 236 mate Experiment data (GRACE, RL06M, Version 2.0) released by the Jet Propulsion Laboratory  
 237 ([Wiese et al., 2016](#)).

### 238 3.4. Comparative mainstream global ET products

239 Six mainstream terrestrial ET products were selected to compare with the ET estimates of the  
 240 SiTHv2 model at a global scale. The terrestrial ET products used in this study were mainly de-  
 241 rived from: 1) the Global Land Evaporation Amsterdam Model (GLEAM), which is a widely used  
 242 process-based ET model ([Martens et al., 2017](#)); 2) the calibration-free complementary relationship  
 243 (CR) model, which is driven by meteorological forcing and is used to calculate ET from the point  
 244 view of atmospheric scope ([Ma et al., 2021](#)); 3) the FLUXCOM initiative product, which is esti-  
 245 mated based on flux observations throughout the globe and a data-driven machine learning method  
 246 ([Jung et al., 2019](#)); 4) the Global Land Data Assimilation System (GLDAS), which was developed  
 247 to assimilate multi-source observations and simulations of land surface models to generate credi-  
 248 ble surface states and fluxes ([Rodell et al., 2004](#)); and 5) ERA5L, which is a cutting-edge global  
 249 reanalysis product with a  $0.1^\circ$  spatial resolution and half-hourly temporal interval ([Muñoz-Sabater  
 250 et al., 2021](#)). Notably, the ET products selected in this study were the most representative models  
 251 or products among the different types of ET estimates.

252 We also used ET simulations from the ensemble mean of the 20 Earth system models in the  
 253 Coupled Model Intercomparison Project Phase 6 (CMIP6) ([Eyring et al., 2016](#)), which is a mission

**Table 2.** Primary global terrestrial ET products used in this study for comparison.

ID <sup>(1)</sup>	Category	Theory	Spatial resolution	Time span	Reference
GLEAM	v3.5a	Remote sensing based model	0.25°	1980–2020	<a href="#">Martens et al. (2017)</a>
CR	v1.0	Complementary relationship	0.25°	1982–2016	<a href="#">Ma et al. (2021)</a>
FluxCom	All ensembles <sup>(2)</sup> in RS_METEO	Machine learning	0.5°	2001–2013	<a href="#">Jung et al. (2019)</a>
CMIP6	Ensemble mean of 20 models <sup>(3)</sup>	Earth system model	0.5°	1979–2014	<a href="#">Eyring et al. (2016)</a>
GLDAS	v2.1/Mosaic LSM	Land surface model	1°	1979–2020	<a href="#">Rodell et al. (2004)</a>
ERA5L	The 5th generation (land component)	Reanalysis/land surface model	0.1°	1950–2021	<a href="#">Muñoz-Sabater et al. (2021)</a>

Note: (1) ID used in this study; (2) all the ensembled latent heat flux estimates of 36 members with energy balance correction; (3) details of the 20 ESMs are provided in the Supplementary information (Table S2).

254 led by the World Climate Research Programme. In contrast to the above-mentioned global ET  
 255 products, these ET simulations were derived by an online Earth system, instead of meteorological  
 256 forcing. The details of these selected products are provided in [Table 2](#).

#### 257 4. Results and Discussions

##### 258 4.1. ET validation at the plot scale using ET observations

259 We validated the ET estimates of the SiTHv2 model at the 175 flux stations and compared the  
 260 results to those of the SiTHv1 model. The Taylor diagrams show the validation results for all the  
 261 individual sites ([Fig. 4a](#)) and for the different PFTs ([Fig. 4b](#)). Moreover, the TS-score was used  
 262 for scoring the model performance, which is a comprehensive indicator derived from the statistics  
 263 of model errors ([Zhu et al., 2016](#)).

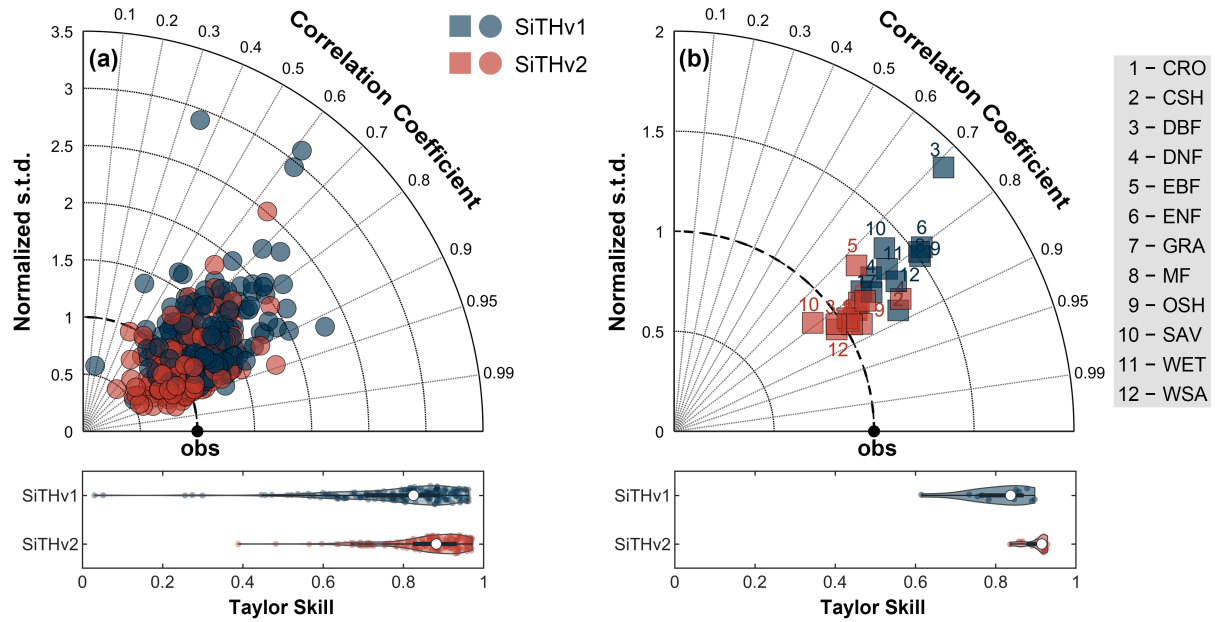


**Fig. 4.** Validation of the ET estimates of the SiTHv2 and SiTHv1 models at individual sites (a) and at the PFT scale (b). The y-axis indicates the normalized standard deviation (N-std) with observed values as the target, the arcs represent the Pearson correlation coefficients ( $R$ ), and the black dot on the x-axis represents the observed benchmark value.

Despite the comparable correlation coefficient ranges, the SiTHv2 model is closer to 1 in terms of the normalized standard deviation (N-std) than the SiTHv1 model (Fig. 4a). The violin plots in the bottom panel demonstrate that the 25th to 75th percentile range of the TS-score for the SiTHv1 model is 0.71 to 0.89, with a median value of 0.82, whereas the 25th to 75th percentile range of the TS-score for the SiTHv2 model is 0.82 to 0.93, with a median value of 0.88. Thus, when all 175 global flux stations are used as a benchmark, the estimated ET of the SiTHv2 model is more in line with the observations, and the TS-score of the SiTHv2 model is approximately 7.3% more than that of the SiTHv1 model. Furthermore, we also aggregated the ET estimates to the PFT scale to test the model performance between SiTHv1 and SiTHv2. Fig. 4b demonstrates that the correlation between the estimated ET of the SiTHv2 model and the observed ET in the various PFTs is stronger than that of the SiTHv1 model (except for EBF and SAV), with  $R$ -values ranging from 0.80 to 0.90. In addition, the results of the SiTHv2 model are more concentrated around the arc with N-std=1, indicating that the ET estimates of the SiTHv2 model are closer to the average

277 of the observations.

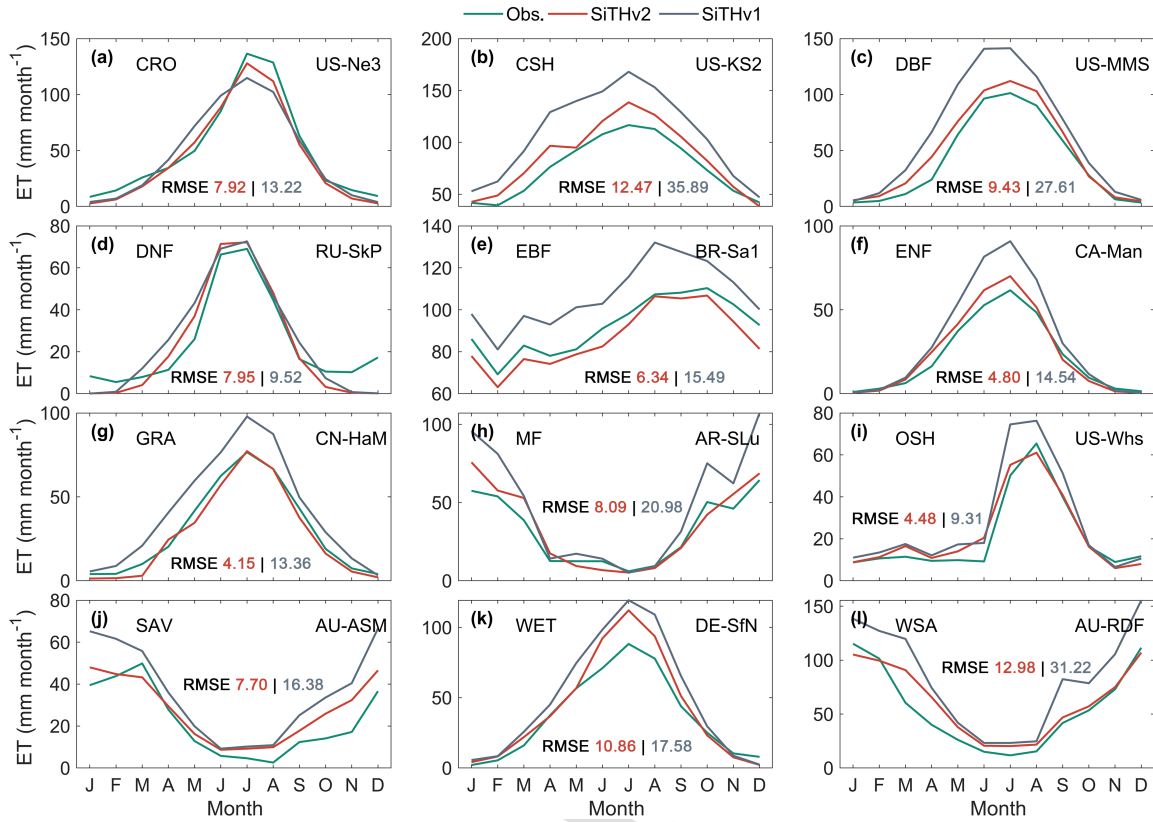


**Fig. 5.** Comparison of the model improvements for typical sites in different PFTs. The green line is the observed ET at each flux site, while the red and gray lines represent the outcomes of the SiTHv2 and SiTHv1 models, respectively.

278 Furthermore, at least one representative site from each PFT was selected to demonstrate the  
 279 superiority of the SiTHv2 model with multi-year monthly averages, which can make the contrast  
 280 in the seasonal variations in model performance even more clearer. As shown in Fig. 5, it is evident  
 281 that the SiTHv2 model improves the ET estimation to various extents for the different PFTs, with  
 282 the reduction of RMSE values ranging from 16.5% (RU-SkP, from 9.52 to 7.95  $\text{mm month}^{-1}$ ) to  
 283 68.9% (CN-HaM, from 13.36 to 4.15  $\text{mm month}^{-1}$ ). This is mostly due to the modified soil water  
 284 constraint scheme implemented in the SiTHv2 model, which accounts for the influence of VOD  
 285 and the relocation of roots in different soil layers, thereby reducing the over-estimation of the old  
 286 version in most cases.

287 To further demonstrate the performance of the new version (SiTHv2), we ran the PT-JPL model

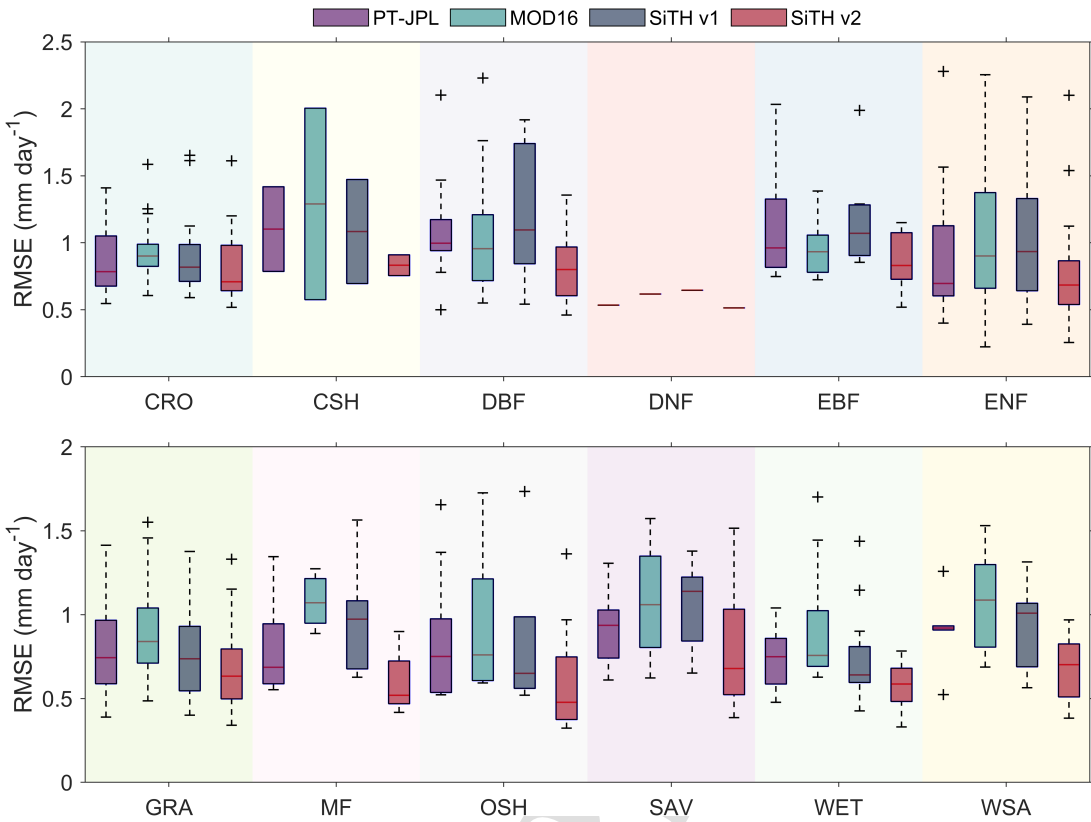


**Fig. 6.** Box plots of the RMSE values when evaluating the modeling results of the SiTHv2, SiTHv1, MOD16, and PT-JPL models against 175 EC stations in different plant functional types.

(Fisher et al., 2008) and the MOD16 model (Mu et al., 2011) on these selected sites and calculated their performance at the PFT level separately (different colored backgrounds) as a side-by-side comparison, in addition to the internal comparison between SiTHv2 and SiTHv1. As shown in Fig. 6, the performance of the different models shows a high degree of PFT-specific variation, which can be attributed to the different model structures. Among the different models, the RMSE of the SiTHv2 model is generally the smallest across the 12 kinds of PFTs, compared to the other models, with the median values ranging from 0.48 to 0.83 mm day<sup>-1</sup>. The average median value of the RMSE in all the PFTs for the SiTHv2 model is 0.66 mm day<sup>-1</sup>, while that for the SiTHv1 model is 0.90 mm day<sup>-1</sup>, which suggests that the overall accuracy of the SiTHv2 model is improved by around 27% when compared to the SiTHv1 model, in terms of RMSE statistics. Furthermore, the performance of the PT-JPL model is close to that of the SiTHv2 model in most

299 PFTs, with an average RMSE median value of  $0.82 \text{ mm day}^{-1}$ . Meanwhile, the MOD16 model  
 300 shows a wide range of variability across the multiple PFTs, with the median value of the RMSE  
 301 ranging from  $0.62$  to  $1.29 \text{ mm day}^{-1}$ , despite it performing better in the DBF and EBF areas.

302 Consequently, based on the ground benchmark of EC observations from a total of 175 flux  
 303 stations, it is confirmed that the SiTHv2 model can provide more accurate ET estimates across the  
 304 different PFTs, compared to the SiTHv1 model, and it also performs well when compared with the  
 305 PT-JPL and MOD16 models.

306 *4.2. ET validation at the basin scale using  $ET_{\text{wb}}$*

307 Unlike the use of ground-based data to validate the performance of models at the plot scale,  
 308 the grid-based terrestrial ET estimates are commonly subject to the limitation of the uncertainty  
 309 for the scale effect, which is caused by the spatial mismatch between the simulated ET grid and  
 310 the ground-based flux footprint. Therefore, we used the independent water-balanced ET data to  
 311 validate the generated ET outputs at the basin scale. As described in Section 3.4, the magnitude of  
 312 the ET in the major global basins was derived from the water balance equation, based on ground  
 313 or remotely sensed observations of runoff, precipitation, and changes in terrestrial water storage.

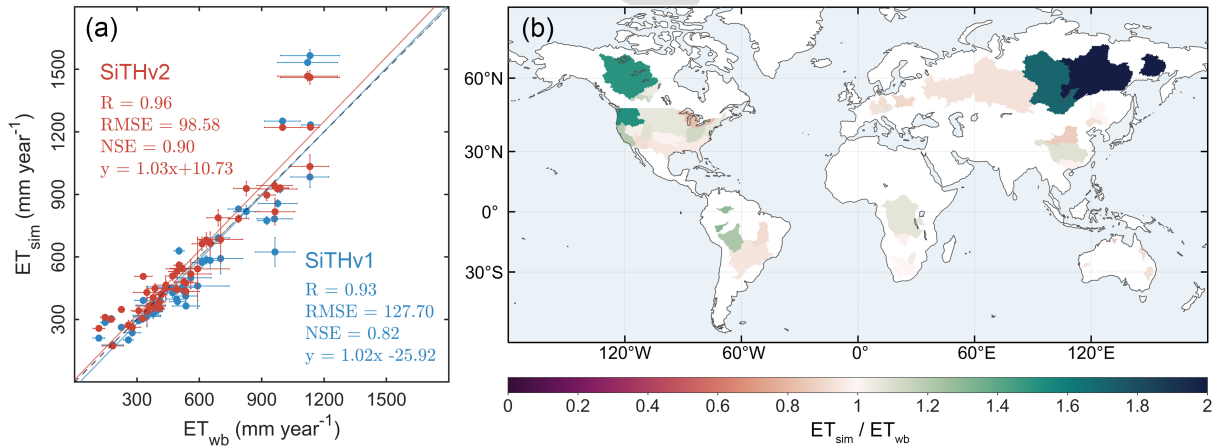


**Fig. 7.** Evaluation of the simulated ET ( $ET_{\text{sim}}$ ) from the SiTHv2 model based on the water-balanced ET ( $ET_{\text{wb}}$ ) at 49 basins over the period of 2003 to 2013 (the same overlapping time span as the other ET products in Fig. 8). (a) Scatter plot between the  $ET_{\text{sim}}$  and  $ET_{\text{wb}}$  with statistics. The unit of RMSE is  $\text{mm year}^{-1}$ . (b) The spatial distribution of the multi-year averaged ET rates relative to the  $ET_{\text{wb}}$  of the 49 basins.

314      Fig. 7a illustrates the scatter plot linear regression between the ET estimates of the SiTHv2  
 315 model (red) and SiTHv1 model (blue) for these basins against the water-balanced ET ( $ET_{wb}$ )  
 316 over the period from 2003 to 2013. It can be found that the ET estimated by the SiTHv2 model  
 317 is generally more consistent with the  $ET_{wb}$  than that estimated by the SiTHv1 model, with a  
 318 higher correlation ( $R = 0.96$ ) and smaller deviation ( $RMSE = 98.58 \text{ mm}\cdot\text{year}^{-1}$ ). Furthermore, the  
 319 SiTHv2 model shows an improvement of nearly 0.1 compared to the SiTHv1 model in terms of  
 320 the Nash-Sutcliffe model efficiency coefficient (NSE).

321      The ratio of the simulated ET (SiTHv2) to  $ET_{wb}$  was also calculated to highlight the spatial  
 322 distribution of the over- or under-estimation of the ET estimates, with  $ET_{wb}$  as the benchmark. In  
 323 the majority of basins, the difference between the estimated ET obtained by the SiTHv2 model  
 324 and  $ET_{wb}$  is fairly minimal, with ratios ranging from 0.8 to 1.2. Meanwhile, it can be found  
 325 that the ET estimated by the SiTHv2 model exhibits a certain degree of over-estimation, of up to  
 326 double the corresponding  $ET_{wb}$  in basins at high latitudes in the Northern Hemisphere (e.g., Siberia  
 327 and northern Canada). Indeed, the freeze-thaw processes at high latitudes have a direct effect on  
 328 soil water content, which in turn influences the ET process (Niu and Yang, 2006). However, the  
 329 current process-based ET model lacks a meaningful connection of the freeze-thaw process and  
 330 the vast amount of measurable data for calibration (such as subsurface ice), which makes accurate  
 331 estimation of ET in these specific regions a challenging task.

332      Moreover, we also selected six mainstream global terrestrial ET products for a side-by-side  
 333 comparison with the SiTHv2 model at the basin scale (Fig. 8). The correlation relationship ( $R$ )  
 334 between all the ET products and  $ET_{wb}$  is very high, with a range of 0.93 to 0.97, which indicates  
 335 the good consistency in the spatial variability of these ET products across the selected basins.  
 336 However, the accuracies of these ET products are relatively diverse, with the GLDAS product  
 337 having the largest RMSE ( $164 \text{ mm year}^{-1}$ ) and the smallest NSE (0.71). In contrast, the CR  
 338 product performs the best, with the smallest RMSE ( $81.83 \text{ mm year}^{-1}$ ) and the largest NSE (0.93)  
 339 among these products, which are similar results to those of the SiTHv2 model obtained in this  
 340 study. Meanwhile, the FluxCom ET product was produced using substantial ground-based flux  
 341 data with machine learning technology, and shows high correlation ( $R = 0.97$ ) with the derived  
 342  $ET_{wb}$  across the different basins. However, this product shows some over-estimation for  $ET_{wb}$

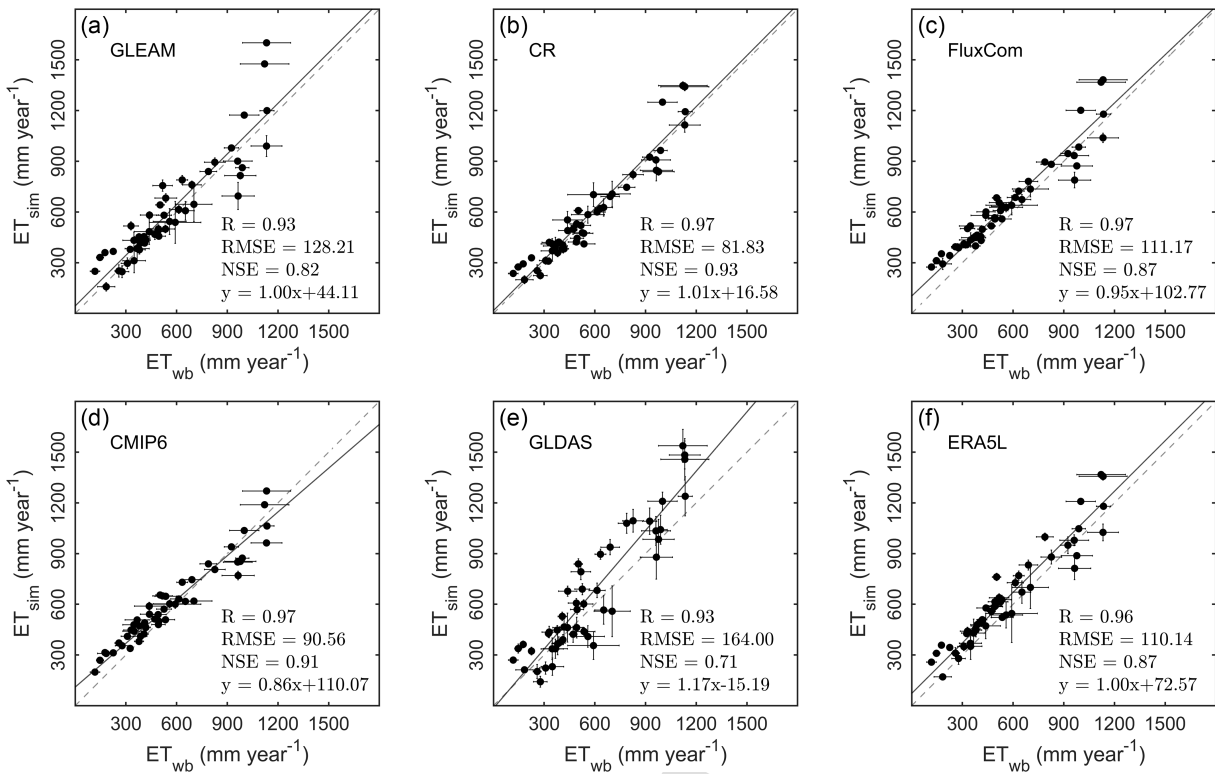


**Fig. 8.** Regression plots of the yearly simulated ET rates from the six primary global ET products relative to the  $ET_{wb}$  at 49 basins during their overlapping temporal coverage from 2003 to 2013. The length of the error bar represents the interannual variability of the ET in each basin. The gray dashed line represents the 1:1 line, while the black line shows the regression line, with the corresponding regression equation shown in the bottom.

in the basins with an arid or cold climate, which are often characterized by low ET values. The performance of the GLEAM product is similar to that of the SiTHv1 model, with an RMSE value of  $128.21 \text{ mm year}^{-1}$  and an NSE value of 0.82. However, the results of the GLEAM product are significantly higher than the results of the other models in basins with a humid climate (e.g., the Amazon region), where the maximum value exceeds  $1500 \text{ mm year}^{-1}$ . In terms of statistical indicators, the CMIP6 product's RMSE ( $90.56 \text{ mm year}^{-1}$ ), R (0.97), and NSE (0.91) values are in the upper-middle level in the overall range, but the lowest slope (0.86) and the largest intercept ( $110.07 \text{ mm year}^{-1}$ ) are found among these model statistics. This indicates that the ET estimates of the CMIP6 product are significantly under-estimated at high values and over-estimated at low values in these basins. The results of the ERA5L product also yield a relatively high NSE value

353 (0.87) and an RMSE value of 110.14 mm year<sup>-1</sup>, which are similar to the results of the FluxCom  
 354 product. Nevertheless, despite the ERA5L product achieving a slope value of 1, its intercept is  
 355 rather large (72.57 mm year<sup>-1</sup>), implying an overall over-estimation in these 49 basins, relative to  
 356  $ET_{wb}$ .

357 It is necessary to emphasize that the different spatial resolutions and production methods of  
 358 these global ET products lead to differences in capturing the spatial details of terrestrial ET, al-  
 359 though their statistical metrics are similar at the basin scale. In general, the terrestrial ET estimated  
 360 by the SiTHv2 model is in good agreement with the  $ET_{wb}$  at the basin scale, and the performance  
 361 is also at a superior level when compared to the primary global ET products available at present.

#### 362 4.3. Global comparison of ET magnitude and trend analysis

363 The global distribution of the multi-year (2001–2018) mean ET estimated by the SiTHv2  
 364 model is displayed in Fig. 9a. The estimated terrestrial ET exhibits a clear and reasonable geo-  
 365 graphical distribution, with the maximum ET appearing in the tropics around the equator (1200–1500  
 366 mm year<sup>-1</sup>), followed by the temperate humid regions (600–1200 mm year<sup>-1</sup>), and then the alpine  
 367 and high-latitude areas (300–600 mm year<sup>-1</sup>), and the lowest ET is found in the desert and ice  
 368 regions (<100 mm year<sup>-1</sup>). The latitudinal profile of the estimated ET derived by the SiTHv2  
 369 model is in close agreement with the highest confidence curve (Fig. 9b), which indicates that the  
 370 SiTHv2 model is effective in capturing the variance in global terrestrial ET at different latitudes.  
 371 However, the ET profile estimated by the SiTHv2 model is positioned lower than that of the other  
 372 ET models in regions south of 40°S. This may be related to the increased uncertainty of the ERA5-  
 373 based precipitation in South America (Xiong et al., 2022), especially since the assimilation system  
 374 hardly corrects the systematic bias in the solid precipitation (i.e., snowfall), due to the insufficient  
 375 observations (Muñoz-Sabater et al., 2021).

376 At the global scale, the magnitude of the total terrestrial ET estimated by the various global  
 377 ET products is a crucial comparative indicator. To compare the estimated terrestrial ET volumes,  
 378 we used the overlapping period from 2001 to 2013, which covers the time span for both the SiTH-  
 379 based ET estimates and the other ET products. As shown in Fig. 10a, the SiTHv2 model estimates  
 380 a total annual mean terrestrial ET of  $70.3 \pm 0.6 \times 10^3$  km<sup>3</sup>, which is very close to the GLEAM

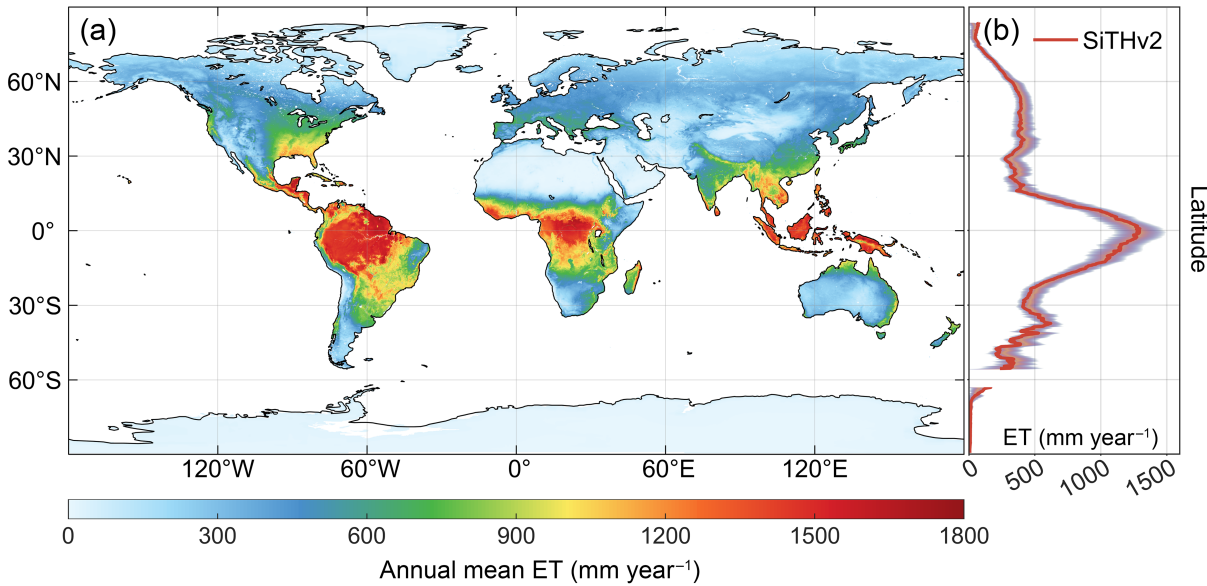


**Fig. 9.** (a) Spatial distribution of the multi-year average terrestrial ET from 2001 to 2018. (b) The latitude-averaged profile of the terrestrial ET corresponds to the panel, where the red line represents the estimates of the SiTHv2 model, and the background range is obtained from the selected primary global ET products (see Table 2), with the gradient color representing the confidence range ( $\pm$  standard deviation) of the different global ET products.

381 estimate ( $70.4 \pm 0.8 \times 10^3$  km<sup>3</sup>) and represents a 6.4% increase over the SiTHv1 model ( $66.1 \pm$   
 382  $0.6 \times 10^3$  km<sup>3</sup>). The results of these three datasets, together with CMIP6, are lower than the  
 383 average value ( $71.5 \times 10^3$  km<sup>3</sup>) of all the selected global ET products, whereas the estimated ET of  
 384 the remaining four products is higher than the average value, with the CR ( $73.0 \pm 0.7 \times 10^3$  km<sup>3</sup>)  
 385 and GLDAS ( $72.1 \pm 3.7 \times 10^3$  km<sup>3</sup>) products being closest to the average, and the FluxCom product  
 386 occupying the highest position ( $77.6 \pm 0.3 \times 10^3$  km<sup>3</sup>). In comparison, the reported volume of the  
 387 terrestrial ET derived from the different models/products in previous studies has primarily ranged  
 388 from  $65 \times 10^3$  km<sup>3</sup> to  $75 \times 10^3$  km<sup>3</sup>, with individual values of  $65.5 \times 10^3$  km<sup>3</sup> (Oki and Kanae,  
 389 2006),  $65 \times 10^3$  km<sup>3</sup> (Jung et al., 2010),  $67.9 \times 10^3$  km<sup>3</sup> (Miralles et al., 2011),  $74.3 \times 10^3$  km<sup>3</sup>  
 390 (Zhang et al., 2015),  $72.8 \times 10^3$  km<sup>3</sup> (Zhang et al., 2019b), and  $71.1 \times 10^3$  km<sup>3</sup> (Zeng et al., 2014).  
 391 More recent studies have tended to yield ET volumes in excess of  $70 \times 10^3$  km<sup>3</sup>. Furthermore,  
 392 the energy balancing strategy seems to be more likely to estimate greater ET volumes, with the  
 393 magnitude of the global terrestrial ET estimate being up to around  $75 \times 10^3$  km<sup>3</sup> (Jung et al., 2019;

394 L'Ecuyer et al., 2015; Wild et al., 2015). In addition, it is worth noting that the time span of the  
 395 above-mentioned ET statistics varies across the different studies.

396 We divided the global terrestrial ET estimates into five main types based on the Köppen cli-  
 397 mate classification system (see Fig. S1 in the Supplementary information), namely, tropical zone,  
 398 dryland zone, temperate zone, continental zone, and polar and alpine zone, to compare the differ-  
 399 ences of the multiple global ET products under the different climatic conditions over the globe.  
 400 The ET volumes estimated by the different products are more or less equivalent to the average  
 401 value ( $32.6 \pm 1.4 \times 10^3 \text{ km}^3$ ) in the tropical zone (Fig. 10b), except for the CMIP6 product, which  
 402 displays obvious under-estimation ( $29.6 \pm 0.1 \times 10^3 \text{ km}^3$ ). However, the performance of the differ-  
 403 ent ET products in the arid zone varies considerably (Fig. 10c), among which the ET estimate from  
 404 the FluxCom product ( $12.9 \pm 0.2 \times 10^3 \text{ km}^3$ ) is the highest, compared to the others. The ERA5L  
 405 and CR products obtain comparable ET volumes in the dryland zone (around  $10 \pm 0.6 \times 10^3 \text{ km}^3$   
 406 to  $10.5 \pm 0.4 \times 10^3 \text{ km}^3$ ), while the result of the SiTHv2 model is similar to that of the GLEAM  
 407 product, with  $8.8 \pm 0.5 \times 10^3 \text{ km}^3$ . Unlike the tropical zone, it is interesting to note that the ET  
 408 estimate of the CMIP6 product is the second highest for the dryland zone, at  $12.5 \pm 0.1 \times 10^3 \text{ km}^3$ .

409 For the temperate zone (Fig. 10d), the ERA5L product shows the highest ET estimate ( $16.3 \pm$   
 410  $0.2 \times 10^3 \text{ km}^3$ ), whereas the lowest ET volume is estimated by the SiTHv1 model ( $13.5 \pm 0.1 \times$   
 411  $10^3 \text{ km}^3$ ). The ET estimates from the FluxCom and GLDAS products in the temperate zone are  
 412 much higher than the overall average, with values of  $16 \pm 0.1 \times 10^3 \text{ km}^3$  and  $15.7 \pm 0.7 \times 10^3 \text{ km}^3$ ,  
 413 respectively. However, the ET estimates from the GLEAM, CR, and CMIP6 products and the  
 414 SiTHv2 model are substantially lower, ranging from  $14.5 \pm 0.1 \times 10^3 \text{ km}^3$  to  $15.0 \pm 0.2 \times 10^3 \text{ km}^3$ .  
 415 In the context of continental climatic conditions with considerable daily and annual air temperature  
 416 variations, the SiTHv1 model tends to under-estimate the volume of ET ( $10.6 \pm 0.2 \times 10^3 \text{ km}^3$ ),  
 417 compared to the other terrestrial ET products (Fig. 10e). In the SiTHv2 model, the estimated  
 418 total ET for the continental climate zone is  $11.8 \pm 0.3 \times 10^3 \text{ km}^3$ , which is comparable to the  
 419  $11.5 \pm 0.1 \times 10^3 \text{ km}^3$  for the CR product and the  $11.7 \pm 0.1 \times 10^3 \text{ km}^3$  for the CMIP6 product.  
 420 The four remaining products generally estimate higher ET values exceeding the average ( $12.2 \pm$   
 421  $0.9 \times 10^3 \text{ km}^3$ ) in the continental climate zone, ranging from  $12.7 \pm 0.2 \times 10^3 \text{ km}^3$  (GLEAM) to  
 422  $13.2 \pm 0.2 \times 10^3 \text{ km}^3$  (ERA5L).

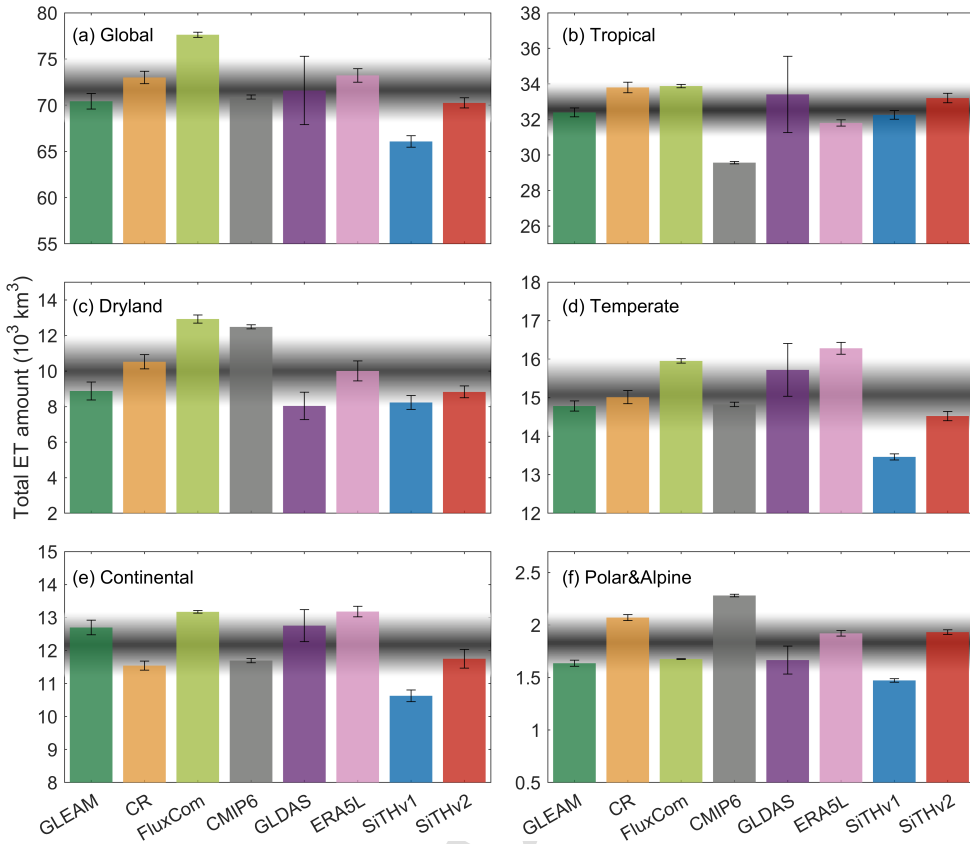


**Fig. 10.** Comparison of the multi-year average terrestrial ET volume for (a) the global scale, (b) the tropical zone, (c) the dryland zone, (d) the temperate zone, (e) the continental zone, and (f) the polar and alpine zone for the period of 2001 to 2013. The error bar represents the standard deviation of the annual values of the ET estimates for each product. The gray gradient range represents the mean of all the products plus/minus their standard deviations. The climate zone classification is in accordance with the Köppen climate classification system.

423     Lastly, the total ET volume in the polar and alpine zone (Fig. 10f) is much lower than in the  
 424 other zones, due to the reduced solar radiation, lower temperature, and lack of vegetation cover.  
 425 Nonetheless, the various ET products exhibit a degree of variability, with the CMIP6 product  
 426 yielding the highest ET volume of  $2.3 \pm 0.01 \times 10^3 \text{ km}^3$ , and the smallest volume of ET is estimated  
 427 by the SiTHv1 model ( $1.47 \pm 0.01 \times 10^3 \text{ km}^3$ ). The ET volume estimated by the SiTHv2 model  
 428 ( $1.93 \pm 0.02 \times 10^3 \text{ km}^3$ ) for the polar and alpine zone is very close to that of the ERA5L product  
 429 ( $1.92 \pm 0.03 \times 10^3 \text{ km}^3$ ). Comparatively, the GLEAM ( $1.64 \pm 0.03 \times 10^3 \text{ km}^3$ ), FluxCom ( $1.68 \pm$   
 430  $0.003 \times 10^3 \text{ km}^3$ ), and GLDAS ( $1.67 \pm 0.1 \times 10^3 \text{ km}^3$ ) products yield similar ET volumes that are

431 slightly less than the overall average ( $1.78 \pm 0.4 \times 10^3 \text{ km}^3$ ) for this zone.

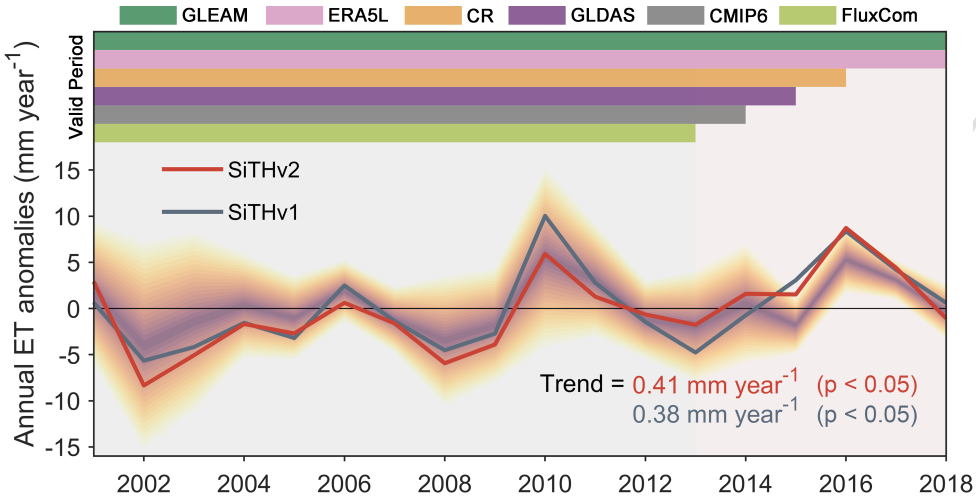


**Fig. 11.** Trends in global terrestrial ET from 2001 to 2018. The red line and gray line represent the trend of the ET anomalies from the SiTHv2 and SiTHv1 models, respectively. The gradually varied interval is the confidence range of the ensemble mean values derived from the multiple ET products, except for SiTH, and the upper panel indicates the valid periods for the products used in this study.

432 The trend of annual global terrestrial ET estimated by the SiTHv2 model from 2011 to 2018 is  
 433  $0.41 \text{ mm year}^{-1}$  ( $p < 0.05$ ), while the trend for the SiTHv1 model is  $0.38 \text{ mm year}^{-1}$  ( $p < 0.05$ )  
 434 (Fig. 11). It should be emphasized that the valid periods for the comparable ET products differ, and  
 435 their overlapping period in this study spans from 2001 to 2013. As a result, the confidence interval  
 436 shrinks after 2013 because of the decreased contribution from the various global ET products.  
 437 Both versions of the SiTH model demonstrate a strong correlation with the ensemble mean of the  
 438 multiple ET products (which excludes the SiTH-based ET estimates), indicating that the anomaly  
 439 trend of the SiTH-based ET is realistic, and can be used to achieve credible trend analysis for  
 440 historical periods. Moreover, the SiTHv2 model is more consistent with the ensemble mean value  
 441 of the multiple ET products in the details, compared to the SiTHv1 model. In summary, the global  
 442 terrestrial ET produced by the SiTHv2 model outperforms that of the SiTHv1 model, and the  
 443 SiTHv2 model can provide reliable ET estimates in terms of global spatial distribution, latitudinal  
 444 profile, and multi-year ET volumes, for both a global scale and the various climate zones, as well  
 445 as the anomaly trend of terrestrial ET.

446 Nonetheless, the SiTHv2 model still has some limitations and deficiencies that will require  
 447 further enhancement in the next stage. Although the current spatial resolution reaches  $0.1^\circ$ , which  
 448 is globally in line with the ERA5L product, a finer spatial resolution is important for local-scale  
 449 applications. To this end, downscaling schemes such as sub-grid optimization could be an efficient  
 450 way to generate finer ET estimates by combining the advantages of multi-source reanalysis and  
 451 satellite forcing data with different spatial resolutions. Also, for the current version, the IWU  
 452 is regarded as additional rainfall only loosely coupled to the SiTHv2 model, which can ensure  
 453 water availability to irrigated regions at the monthly/yearly scale (limited by the monthly IWU  
 454 estimates), but makes it difficult to characterize the irrigation recharge at a fine temporal scale.  
 455 Together with the challenge of representing specific irrigation modes, i.e., sprinkler, drip, or flood  
 456 irrigation, these factors will increase the uncertainty in the simulation of soil water dynamics.  
 457 Hence, to assimilate satellite-based soil moisture into the simulation would be a more direct way  
 458 of characterizing realistic surface water conditions, and further improving cropland ET estimation.  
 459 In addition, the current model is only applied to the simulation in the vertical direction, without the  
 460 interaction from the neighboring grids. By introducing topographic factors (e.g., elevation, slope,  
 461 and aspect) to describe the lateral water flow between adjacent grid cells, this would enhance the  
 462 simulation of the SiTHv2 model to three dimensions, and could thus greatly expand the application  
 463 potential at the basin level.

## 464 5. Conclusions

465 This study was dedicated to improving the ET simulation in the SiTH model within the GSPAC.  
 466 We enhanced the vegetation moisture constraint module by coupling satellite-based VOD mea-  
 467 surements. Moreover, a dynamic adjustment scheme for the critical threshold of soil water content  
 468 based on different canopy heights and specific environmental conditions was applied in the SiTHv2  
 469 model. The extended soil layer with re-optimized root distribution parameters was used to better  
 470 characterize the effect of soil water dynamics on the ET simulation. We also added an irrigation  
 471 water strategy as extra input water applied in the croplands zone. In addition, the meteorological  
 472 forcing data in the SiTHv2 model were updated to the state-of-the-art ERA5L reanalysis product.

473 Validations against 175 EC stations and water balance data from 49 large river basins suggested

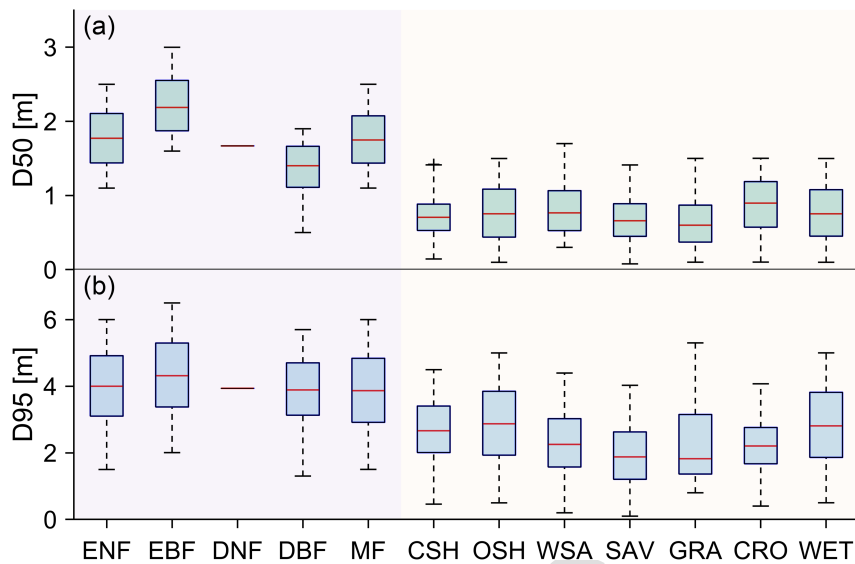
474 that the SiTHv2 model is more accurate and has less uncertainty than the SiTHv1 model at both  
475 plot and basin scales. Further multi-product evaluations using the water balance approach also  
476 demonstrated that the SiTHv2 model ranks well when compared to most of the mainstream ET  
477 products. Lastly, a side-by-side comparison at the global scale indicated that the SiTHv2 model  
478 is consistent with the ensemble mean results of the multiple terrestrial ET products, both in terms  
479 of magnitude and trends. This newly improved SiTH model will provide the necessary framework  
480 for estimating ET from the GSPAC, and will promote better support for exploring land-atmosphere  
481 feedback loops, ecosystem water consumption, and related ecohydrological studies.

482 **Declaration of Competing Interest**

483 The authors declare that they have no known competing financial interests or personal rela-  
484 tionships that could have appeared to influence the work reported in this paper.

485 **Acknowledgments**

486 This work was supported by the National Natural Science Foundation of China (grant nos.  
487 41901381, 41871078, 41801047, and 42171019). We appreciate the anonymous reviewers, and  
488 the Editor for their constructive and detailed comments on this paper. We are also grateful to the  
489 principal investigators and their teams for all the datasets used in this study. The generated global  
490 terrestrial ET dataset of the SiTHv2 model can be achieved from the National Tibetan Plateau Data  
491 Center (TPDC) at <http://dx.doi.org/10.11888/Atmos.tpdc.272728>

492 **Appendix A. Posterior distribution of D50 and D95**

**Fig. A1.** Posterior distributions of D50 and D95 in the different PFTs. The boxes represent the 75% credible interval, and the horizontal line represents the median value.

493 **Appendix B. Supplementary data**

494      Supplementary data to this article can be found at the online version.

495 **References**

- 496 Allen, R.G., Pereira, L.S., Howell, T.A., Jensen, M.E., 2011. Evapotranspiration information reporting: I. factors  
497 governing measurement accuracy. Agricultural Water Management 98, 899–920. doi:10.1016/j.agwat.2010.  
498 12.015.
- 499 Beer, A., 1852. Bestimmung der absorption des rothen lichts in farbigen flüssigkeiten. Ann. Physik 162, 78–88.
- 500 Canadell, J., Jackson, R.B., Ehleringer, J.B., Mooney, H.A., Sala, O.E., Schulze, E.D., 1996. Maximum rooting depth  
501 of vegetation types at the global scale. Oecologia 108, 583–595. doi:10.1007/BF00329030.
- 502 Chen, H., Zhu, G., Shang, S., Qin, W., Zhang, Y., Su, Y., Zhang, K., Zhu, Y., Xu, C., 2022. Uncertainties in  
503 partitioning evapotranspiration by two remote sensing-based models. Journal of Hydrology 604, 127223. doi:10.  
504 1016/j.jhydrol.2021.127223.
- 505 Chen, H., Zhu, G., Zhang, K., Bi, J., Jia, X., Ding, B., Zhang, Y., Shang, S., Zhao, N., Qin, W., 2020. Evaluation of  
506 evapotranspiration models using different lai and meteorological forcing data from 1982 to 2017. Remote Sensing  
507 12, 2473. doi:10.3390/rs12152473.

- 508 Daly, C., Halbleib, M., Smith, J.I., Gibson, W.P., Doggett, M.K., Taylor, G.H., Curtis, J., Pasteris, P.P., 2008. Phys-  
 509 iographically sensitive mapping of climatological temperature and precipitation across the conterminous United  
 510 States. *International Journal of Climatology* 28, 2031–2064. doi:10.1002/joc.1688.
- 511 van Diepen, C., Wolf, J., van Keulen, H., Rappoldt, C., 1989. Wofost: a simulation model of crop production. *Soil*  
 512 *Use and Management* 5, 16–24. doi:10.1111/j.1475-2743.1989.tb00755.x.
- 513 Dorigo, W., Dietrich, S., Aires, F., Brocca, L., Carter, S., Cretaux, J.F., Dunkerley, D., Enomoto, H., Forsberg, R.,  
 514 Güntner, A., Hegglin, M.I., Hollmann, R., Hurst, D.F., Johannessen, J.A., Kummerow, C., Lee, T., LuoJus, K.,  
 515 Looser, U., Miralles, D.G., Pellet, V., Recknagel, T., Vargas, C.R., Schneider, U., Schoeneich, P., Schröder, M.,  
 516 Tapper, N., Vuglinsky, V., Wagner, W., Yu, L., Zappa, L., Zemp, M., Aich, V., 2021. Closing the water cycle  
 517 from observations across scales: Where do we stand? *Bulletin of the American Meteorological Society* 102,  
 518 E1897–E1935. doi:10.1175/BAMS-D-19-0316.1.
- 519 Eyring, V., Bony, S., Meehl, G.A., Senior, C.A., Stevens, B., Stouffer, R.J., Taylor, K.E., 2016. Overview of the  
 520 coupled model intercomparison project phase 6 (cmip6) experimental design and organization. *Geoscientific Model*  
 521 *Development* 9, 1937–1958. doi:10.5194/gmd-9-1937-2016.
- 522 Fan, Y., 2015. Groundwater in the earth's critical zone: Relevance to large-scale patterns and processes. *Water*  
 523 *Resources Research* 51, 3052–3069. doi:10.1002/2015WR017037.
- 524 Fisher, J.B., Tu, K.P., Baldocchi, D.D., 2008. Global estimates of the land–atmosphere water flux based on monthly  
 525 avhrr and islscp-ii data, validated at 16 fluxnet sites. *Remote Sensing of Environment* 112, 901–919. doi:10.  
 526 1016/j.rse.2007.06.025.
- 527 Foley, J.A., Ramankutty, N., Brauman, K.A., Cassidy, E.S., Gerber, J.S., Johnston, M., Mueller, N.D., O'Connell, C.,  
 528 Ray, D.K., West, P.C., Balzer, C., Bennett, E.M., Carpenter, S.R., Hill, J., Monfreda, C., Polasky, S., Rockström,  
 529 J., Sheehan, J., Siebert, S., Tilman, D., Zaks, D.P.M., 2011. Solutions for a cultivated planet. *Nature* 478, 337–342.  
 530 doi:10/fptzqk.
- 531 Frankenberg, C., Fisher, J.B., Worden, J., Badgley, G., Saatchi, S.S., Lee, J.E., Toon, G.C., Butz, A., Jung, M.,  
 532 Kuze, A., Yokota, T., 2011. New global observations of the terrestrial carbon cycle from gosat: Patterns of plant  
 533 fluorescence with gross primary productivity. *Geophysical Research Letters* 38. doi:10.1029/2011GL048738.
- 534 Gou, S., Miller, G., 2014. A groundwater–soil–plant–atmosphere continuum approach for modelling water stress,  
 535 uptake, and hydraulic redistribution in phreatophytic vegetation. *Ecohydrology* 7, 1029–1041. doi:10.1002/eco.  
 536 1427.
- 537 Held, I.M., Soden, B.J., 2006. Robust responses of the hydrological cycle to global warming. *Journal of Climate* 19,  
 538 5686–5699. doi:10.1175/JCLI3990.1.
- 539 Impens, I., Lemeur, R., 1969. Extinction of net radiation in different crop canopies. *Archiv für Meteorologie,*  
 540 *Geophysik und Bioklimatologie, Serie B* 17, 403–412.
- 541 Jackson, T.J., Schmugge, T.J., 1991. Vegetation effects on the microwave emission of soils. *Remote Sensing of*

- 542 Environment 36, 203–212. doi:10.1016/0034-4257(91)90057-D.
- 543 Jasechko, S., Sharp, Z.D., Gibson, J.J., Birks, S.J., Yi, Y., Fawcett, P.J., 2013. Terrestrial water fluxes dominated by  
544 transpiration. Nature 496, 347–350. doi:10.1038/nature11983.
- 545 Jung, M., Koitala, S., Weber, U., Ichii, K., Gans, F., Camps-Valls, G., Papale, D., Schwalm, C., Tramontana, G.,  
546 Reichstein, M., 2019. The fluxcom ensemble of global land-atmosphere energy fluxes. Scientific Data 6, 74.  
547 doi:10.1038/s41597-019-0076-8.
- 548 Jung, M., Reichstein, M., Ciais, P., Seneviratne, S.I., Sheffield, J., Goulden, M.L., Bonan, G., Cescatti, A., Chen,  
549 J., de Jeu, R., Dolman, A.J., Eugster, W., Gerten, D., Gianelle, D., Gobron, N., Heinke, J., Kimball, J., Law,  
550 B.E., Montagnani, L., Mu, Q., Mueller, B., Oleson, K., Papale, D., Richardson, A.D., Roupsard, O., Running,  
551 S., Tomelleri, E., Viovy, N., Weber, U., Williams, C., Wood, E., Zaehle, S., Zhang, K., 2010. Recent decline  
552 in the global land evapotranspiration trend due to limited moisture supply. Nature 467, 951–954. doi:10.1038/  
553 nature09396.
- 554 Kato, S., Rose, F.G., Rutan, D.A., Thorsen, T.J., Loeb, N.G., Doelling, D.R., Huang, X., Smith, W.L., Su, W., Ham,  
555 S.H., 2018. Surface irradiances of edition 4.0 clouds and the earth's radiant energy system (ceres) energy balanced  
556 and filled (ebaf) data product. Journal of Climate 31, 4501–4527. doi:10.1175/JCLI-D-17-0523.1.
- 557 L'Ecuyer, T.S., Beaudoing, H.K., Rodell, M., Olson, W., Lin, B., Kato, S., Clayson, C.A., Wood, E., Sheffield, J.,  
558 Adler, R., Huffman, G., Bosilovich, M., Gu, G., Robertson, F., Houser, P.R., Chambers, D., Famiglietti, J.S.,  
559 Fetzer, E., Liu, W.T., Gao, X., Schlosser, C.A., Clark, E., Lettenmaier, D.P., Hilburn, K., 2015. The observed  
560 state of the energy budget in the early twenty-first century. Journal of Climate 28, 8319–8346. doi:10.1175/  
561 JCLI-D-14-00556.1.
- 562 Liang, S., Cheng, J., Jia, K., Jiang, B., Liu, Q., Xiao, Z., Yao, Y., Yuan, W., Zhang, X., Zhao, X., Zhou, J., 2021. The  
563 global land surface satellite (glass) product suite. Bulletin of the American Meteorological Society 102, E323–  
564 E337. doi:10.1175/BAMS-D-18-0341.1.
- 565 Liu, Y.Y., van Dijk, A.I.J.M., de Jeu, R.A.M., Canadell, J.G., McCabe, M.F., Evans, J.P., Wang, G., 2015. Recent  
566 reversal in loss of global terrestrial biomass. Nature Climate Change 5, 470–474. doi:10.1038/nclimate2581.
- 567 Liu, Y.Y., de Jeu, R.A.M., McCabe, M.F., Evans, J.P., van Dijk, A.I.J.M., 2011. Global long-term passive microwave  
568 satellite-based retrievals of vegetation optical depth. Geophysical Research Letters 38. URL: <http://onlinelibrary.wiley.com/doi/abs/10.1029/2011GL048684>. doi:10.1029/2011GL048684.
- 569 Lundquist, J.D., Hughes, M., Henn, B., Gutmann, E.D., Livneh, B., Dozier, J., Neiman, P., 2015. High-elevation pre-  
570 precipitation patterns: Using snow measurements to assess daily gridded datasets across the sierra nevada, california.  
571 Journal of Hydrometeorology 16, 1773–1792. doi:10.1175/JHM-D-15-0019.1.
- 572 Ma, N., Szilagyi, J., Zhang, Y., 2021. Calibration-free complementary relationship estimates terrestrial evapotranspi-  
573 ration globally. Water Resources Research 57, e2021WR029691. doi:10.1029/2021WR029691.
- 574 Ma, N., Szilagyi, J., Zhang, Y., Liu, W., 2019. Complementary-Relationship-Based Modeling of Terrestrial Evapo-

- 576 transpiration Across China During 1982–2012: Validations and Spatiotemporal Analyses. *Journal of Geophysical*  
 577 *Research: Atmospheres* 124, 4326–4351. doi:10.1029/2018JD029850.
- 578 Ma, N., Zhang, Y., 2022. Increasing tibetan plateau terrestrial evapotranspiration primarily driven by precipitation.  
 579 *Agricultural and Forest Meteorology* 317, 108887. doi:10.1016/j.agrformet.2022.108887.
- 580 Maeght, J.L., Rewald, B., Pierret, A., 2013. How to study deep roots—and why it matters. *Frontiers in Plant Science*  
 581 4. URL: <https://www.frontiersin.org/article/10.3389/fpls.2013.00299>, doi:10.3389/fpls.2013.00299.
- 582 Martens, B., Miralles, D.G., Lievens, H., van der Schalie, R., de Jeu, R.A.M., Fernández-Prieto, D., Beck, H.E.,  
 583 Dorigo, W.A., Verhoest, N.E.C., 2017. Gleam v3: satellite-based land evaporation and root-zone soil moisture.  
 584 *Geoscientific Model Development* 10, 1903–1925. doi:10.5194/gmd-10-1903-2017.
- 585 Miralles, D.G., De Jeu, R.A.M., Gash, J.H., Holmes, T.R.H., Dolman, A.J., 2011. Magnitude and variability of  
 586 land evaporation and its components at the global scale. *Hydrology and Earth System Sciences* 15, 967–981.  
 587 doi:10.5194/hess-15-967-2011.
- 588 Miralles, D.G., Gentine, P., Seneviratne, S.I., Teuling, A.J., 2019. Land-atmospheric feedbacks during droughts and  
 589 heatwaves: state of the science and current challenges. *Annals of the New York Academy of Sciences* 1436, 19–35.  
 590 doi:10.1111/nyas.13912.
- 591 Moesinger, L., Dorigo, W., de Jeu, R., van der Schalie, R., Scanlon, T., Teubner, I., Forkel, M., 2020. The global  
 592 long-term microwave vegetation optical depth climate archive (vodca). *Earth System Science Data* 12, 177–196.  
 593 doi:10.5194/essd-12-177-2020.
- 594 Mu, Q., Zhao, M., Running, S.W., 2011. Improvements to a modis global terrestrial evapotranspiration algorithm.  
 595 *Remote Sensing of Environment* 115, 1781–1800. doi:10.1016/j.rse.2011.02.019.
- 596 Muñoz-Sabater, J., Dutra, E., Agustí-Panareda, A., Albergel, C., Arduini, G., Balsamo, G., Boussetta, S., Choulga,  
 597 M., Harrigan, S., Hersbach, H., Martens, B., Miralles, D.G., Piles, M., Rodríguez-Fernández, N.J., Zsoter, E.,  
 598 Buontempo, C., Thépaut, J.N., 2021. Era5-land: a state-of-the-art global reanalysis dataset for land applications.  
 599 *Earth System Science Data* 13, 4349–4383. doi:10.5194/essd-13-4349-2021.
- 600 Niu, G.Y., Yang, Z.L., 2006. Effects of frozen soil on snowmelt runoff and soil water storage at a continental scale.  
 601 *Journal of Hydrometeorology* 7, 937–952. doi:10.1175/JHM538.1.
- 602 Oki, T., Kanae, S., 2006. Global hydrological cycles and world water resources. *Science* 313, 1068. doi:10.1126/  
 603 science.1128845.
- 604 Owe, M., Jeu, d.R., Holmes, T., 2008. Multisensor historical climatology of satellite-derived global land surface  
 605 moisture. *Journal of Geophysical Research: Earth Surface* 113. URL: <https://agupubs.onlinelibrary.wiley.com/doi/abs/10.1029/2007JF000769>, doi:10.1029/2007JF000769.
- 607 Pan, S., Pan, N., Tian, H., Friedlingstein, P., Sitch, S., Shi, H., Arora, V.K., Haverd, V., Jain, A.K., Kato, E., Liener, S.,  
 608 Lombardozzi, D., Nabel, J.E.M.S., Ottlé, C., Poulter, B., Zaehle, S., Running, S.W., 2020. Evaluation of  
 609 global terrestrial evapotranspiration using state-of-the-art approaches in remote sensing, machine learning and land

surface modeling. *Hydrology and Earth System Sciences* 24, 1485–1509. doi:10.5194/hess-24-1485-2020.

Pastorello, G., Trotta, C., Canfora, E., Chu, H., Christianson, D., Cheah, Y.W., Poindexter, C., Chen, J., Elbashandy, A., Humphrey, M., Isaac, P., Polidori, D., Reichstein, M., Ribeca, A., van Ingen, C., Vuichard, N., Zhang, L., Amiro, B., Ammann, C., Arain, M.A., Ardö, J., Arkebauer, T., Arndt, S.K., Arriga, N., Aubinet, M., Aurela, M., Baldocchi, D., Barr, A., Beamesderfer, E., Marchesini, L.B., Bergeron, O., Beringer, J., Bernhofer, C., Berveiller, D., Billesbach, D., Black, T.A., Blanken, P.D., Bohrer, G., Boike, J., Bolstad, P.V., Bonal, D., Bonnefond, J.M., Bowling, D.R., Bracho, R., Brodeur, J., Brümmer, C., Buchmann, N., Burban, B., Burns, S.P., Buysse, P., Cale, P., Cavagna, M., Cellier, P., Chen, S., Chini, I., Christensen, T.R., Cleverly, J., Collalti, A., Consalvo, C., Cook, B.D., Cook, D., Coursolle, C., Cremonese, E., Curtis, P.S., D'Andrea, E., da Rocha, H., Dai, X., Davis, K.J., Cinti, B.D., Grandcourt, d.A., Ligne, A.D., De Oliveira, R.C., Delpierre, N., Desai, A.R., Di Bella, C.M., Tommasi, d.P., Dolman, H., Domingo, F., Dong, G., Dore, S., Duce, P., Dufrêne, E., Dunn, A., Dušek, J., Eamus, D., Eichelmann, U., ElKhidir, H.A.M., Eugster, W., Ewenz, C.M., Ewers, B., Famulari, D., Fares, S., Feigenwinter, I., Feitz, A., Fensholt, R., Filippa, G., Fischer, M., Frank, J., Galvagno, M., Gharun, M., Gianelle, D., Gielen, B., Gioli, B., Gitelson, A., Goded, I., Goeckede, M., Goldstein, A.H., Gough, C.M., Goulden, M.L., Graf, A., Griebel, A., Gruening, C., Grünwald, T., Hammerle, A., Han, S., Han, X., Hansen, B.U., Hanson, C., Hatakka, J., He, Y., Hehn, M., Heinesch, B., Hinko-Najera, N., Hörtnagl, L., Hutley, L., Ibrom, A., Ikawa, H., Jackowicz-Korczynski, M., Janouš, D., Jans, W., Jassal, R., Jiang, S., Kato, T., Khomik, M., Klatt, J., Knohl, A., Knox, S., Kobayashi, H., Koerber, G., Kolle, O., Kosugi, Y., Kotani, A., Kowalski, A., Kruijt, B., Kurbatova, J., Kutsch, W.L., Kwon, H., Launiainen, S., Laurila, T., Law, B., Leuning, R., Li, Y., Liddell, M., Limousin, J.M., Lion, M., Liska, A.J., Lohila, A., López-Ballesteros, A., López-Blanco, E., Loubet, B., Loustau, D., Lucas-Moffat, A., Lüers, J., Ma, S., Macfarlane, C., Magliulo, V., Maier, R., Mammarella, I., Manca, G., Marcolla, B., Margolis, H.A., Marras, S., Massman, W., Mastepanov, M., Matamala, R., Matthes, J.H., Mazzenga, F., McCaughey, H., McHugh, I., McMillan, A.M.S., Merbold, L., Meyer, W., Meyers, T., Miller, S.D., Minerbi, S., Moderow, U., Monson, R.K., Montagnani, L., Moore, C.E., Moors, E., Moreaux, V., Moureaux, C., Munger, J.W., Nakai, T., Neirynck, J., Nesic, Z., Nicolini, G., Noormets, A., Northwood, M., Nosetto, M., Nouvellon, Y., Novick, K., Oechel, W., Olesen, J.E., Ourcival, J.M., Papuga, S.A., Parmentier, F.J., Paul-Limoges, E., Pavelka, M., Peichl, M., Pendall, E., Phillips, R.P., Pilegaard, K., Pirk, N., Posse, G., Powell, T., Prasse, H., Prober, S.M., Rambal, S., Rannik, U., Raz-Yaseef, N., Rebmann, C., Reed, D., Dios, d.V.R., Restrepo-Coupe, N., Reverter, B.R., Roland, M., Sabbatini, S., Sachs, T., Saleska, S.R., Sánchez-Cañete, E.P., Sanchez-Mejia, Z.M., Schmid, H.P., Schmidt, M., Schneider, K., Schrader, F., Schroder, I., Scott, R.L., Sedláček, P., Serrano-Ortíz, P., Shao, C., Shi, P., Shironya, I., Siebicke, L., Šigut, L., Silberstein, R., Sirca, C., Spano, D., Steinbrecher, R., Stevens, R.M., Sturtevant, C., Suyker, A., Tagesson, T., Takanashi, S., Tang, Y., Tapper, N., Thom, J., Tomassucci, M., Tuovinen, J.P., Urbanski, S., Valentini, R., van der Molen, M., van Gorsel, E., van Huissteden, K., Varlagin, A., Verfaillie, J., Vesala, T., Vincke, C., Vitale, D., Vygodskaya, N., Walker, J.P., Walter-Shea, E., Wang, H., Weber, R., Westermann, S., Wille, C., Wofsy, S.,

- 644 Wohlfahrt, G., Wolf, S., Woodgate, W., Li, Y., Zampedri, R., Zhang, J., Zhou, G., Zona, D., Agarwal, D., Biraud,  
 645 S., Torn, M., Papale, D., 2020. The fluxnet2015 dataset and the oneflux processing pipeline for eddy covariance  
 646 data. *Scientific Data* 7, 225. doi:10.1038/s41597-020-0534-3.
- 647 Purdy, A.J., Fisher, J.B., Goulden, M.L., Colliander, A., Halverson, G., Tu, K., Famiglietti, J.S., 2018. Smap soil  
 648 moisture improves global evapotranspiration. *Remote Sensing of Environment* 219, 1–14. doi:10.1016/j.rse.  
 649 2018.09.023.
- 650 Rodell, M., Houser, P.R., Jambor, U., Gottschalck, J., Mitchell, K., Meng, C.J., Arsenault, K., Cosgrove, B.,  
 651 Radakovich, J., Bosilovich, M., Entin, J.K., Walker, J.P., Lohmann, D., Toll, D., 2004. The global land data assim-  
 652 ilation system. *Bulletin of the American Meteorological Society* 85, 381–394. doi:10.1175/BAMS-85-3-381.
- 653 Scanlon, T.M., Kustas, W.P., 2012. Partitioning evapotranspiration using an eddy covariance-based technique:  
 654 Improved assessment of soil moisture and land–atmosphere exchange dynamics. *Vadose Zone Journal* 11,  
 655 vzzj2012.0025. doi:10.2136/vzzj2012.0025.
- 656 Schneider, U., Becker, A., Finger, P., Meyer-Christoffer, A., Ziese, M., 2018. Gpcc full data monthly product version  
 657 2018 at 0.5 degree: monthly land-surface precipitation from rain-gauges built on gts-based and historical data.  
 658 Global Precipitation Climatology Centre doi:10.5676/DWD\_GPCC/FD\_M\_V2018\_025.
- 659 Schwingshackl, C., Hirschi, M., Seneviratne, S.I., 2017. Quantifying spatiotemporal variations of soil moisture  
 660 control on surface energy balance and near-surface air temperature. *Journal of Climate* 30, 7105–7124. doi:10.  
 661 1175/JCLI-D-16-0727.1.
- 662 Siebert, S., Döll, P., 2010. Quantifying blue and green virtual water contents in global crop production as well as  
 663 potential production losses without irrigation. *Journal of Hydrology* 384, 198–217. doi:10.1016/j.jhydrol.  
 664 2009.07.031.
- 665 Sulla-Menashe, D., Gray, J.M., Abercrombie, S.P., Friedl, M.A., 2019. Hierarchical mapping of annual global land  
 666 cover 2001 to present: The modis collection 6 land cover product. *Remote Sensing of Environment* 222, 183–194.  
 667 doi:10.1016/j.rse.2018.12.013.
- 668 Ter Braak, C.J.F., Vrugt, J.A., 2008. Differential evolution markov chain with snooker updater and fewer chains.  
 669 *Statistics and Computing* 18, 435–446. doi:10.1007/s11222-008-9104-9.
- 670 Teuling, A.J., Seneviratne, S.I., Stöckli, R., Reichstein, M., Moors, E., Ciais, P., Luyssaert, S., van den Hurk, B.,  
 671 Ammann, C., Bernhofer, C., Dellwik, E., Gianelle, D., Gielen, B., Grünwald, T., Klumpp, K., Montagnani, L.,  
 672 Moureaux, C., Sottocornola, M., Wohlfahrt, G., 2010. Contrasting response of european forest and grassland  
 673 energy exchange to heatwaves. *Nature Geoscience* 3, 722–727. doi:10.1038/ngeo950.
- 674 Trenberth, K.E., Fasullo, J.T., Kiehl, J., 2009. Earth's global energy budget. *Bulletin of the American Meteorological  
 675 Society* 90, 311–324. doi:10.1175/2008BAMS2634.1.
- 676 Wang, K., Dickinson, R.E., 2012. A review of global terrestrial evapotranspiration: Observation, modeling, climatol-  
 677 ogy, and climatic variability. *Reviews of Geophysics* 50. doi:10.1029/2011RG000373.

- 678 Wang, Y., Zhou, J., Ma, R., Zhu, G., Zhang, Y., 2022. Development of a new pedotransfer function addressing  
 679 limitations in soil hydraulic models and observations. *Water Resources Research* 58, e2021WR031406. doi:10.  
 680 1029/2021WR031406.
- 681 Wieder, W., Boehnert, J., Bonan, G., Langseth, M., 2014. Regridded harmonized world soil database v1. 2. ORNL  
 682 DAAC .
- 683 Wiese, D.N., Landerer, F.W., Watkins, M.M., 2016. Quantifying and reducing leakage errors in the jpl rl05m grace  
 684 mascon solution. *Water Resources Research* 52, 7490–7502. doi:10.1002/2016WR019344.
- 685 Wild, M., Folini, D., Hakuba, M.Z., Schär, C., Seneviratne, S.I., Kato, S., Rutan, D., Ammann, C., Wood, E.F.,  
 686 König-Langlo, G., 2015. The energy balance over land and oceans: an assessment based on direct observations  
 687 and cmip5 climate models. *Climate Dynamics* 44, 3393–3429. doi:10.1007/s00382-014-2430-z.
- 688 Xiong, W., Tang, G., Wang, T., Ma, Z., Wan, W., 2022. Evaluation of imerg and era5 precipitation-phase partitioning  
 689 on the global scale. *Water* 14, 1122. doi:10.3390/w14071122.
- 690 Xu, Z., Chen, X., Liu, J., Zhang, Y., Chau, S., Bhattacharai, N., Wang, Y., Li, Y., Connor, T., Li, Y., 2020. Impacts of  
 691 irrigated agriculture on food–energy–water–co<sub>2</sub> nexus across metacoupled systems. *Nature Communications* 11,  
 692 5837. doi:10.1038/s41467-020-19520-3.
- 693 Zeng, Z., Wang, T., Zhou, F., Ciais, P., Mao, J., Shi, X., Piao, S., 2014. A worldwide analysis of spatiotemporal  
 694 changes in water balance-based evapotranspiration from 1982 to 2009. *Journal of Geophysical Research: Atmo-*  
 695 *spheres* 119, 1186–1202. doi:10.1002/2013JD020941.
- 696 Zhang, K., Kimball, J.S., Nemani, R.R., Running, S.W., Hong, Y., Gourley, J.J., Yu, Z., 2015. Vegetation greening  
 697 and climate change promote multidecadal rises of global land evapotranspiration. *Scientific Reports* 5, 75–77.  
 698 doi:10.1038/srep15956.
- 699 Zhang, K., Li, X., Zheng, D., Zhang, L., Zhu, G., 2022. Estimation of global irrigation water use by the integration of  
 700 multiple satellite observations. *Water Resources Research* 58, e2021WR030031. doi:10.1029/2021WR030031.
- 701 Zhang, K., Ma, J., Zhu, G., Ma, T., Han, T., Feng, L.L., 2017. Parameter sensitivity analysis and optimization for a  
 702 satellite-based evapotranspiration model across multiple sites using moderate resolution imaging spectroradiometer  
 703 and flux data. *Journal of Geophysical Research: Atmospheres* 122, 230–245. doi:10.1002/2016JD025768.
- 704 Zhang, K., Zhu, G., Ma, J., Yang, Y., Shang, S., Gu, C., 2019a. Parameter analysis and estimates for the modis  
 705 evapotranspiration algorithm and multiscale verification. *Water Resources Research* 55, 2211–2231. doi:10.  
 706 1029/2018WR023485.
- 707 Zhang, Y., Kong, D., Gan, R., Chiew, F.H.S., McVicar, T.R., Zhang, Q., Yang, Y., 2019b. Coupled estimation of 500  
 708 m and 8-day resolution global evapotranspiration and gross primary production in 2002–2017. *Remote Sensing of*  
 709 *Environment* 222, 165–182. doi:10.1016/j.rse.2018.12.031.
- 710 Zhang, Y., Peña-Arancibia, J.L., McVicar, T.R., Chiew, F.H.S., Vaze, J., Liu, C., Lu, X., Zheng, H., Wang, Y.,  
 711 Liu, Y.Y., Miralles, D.G., Pan, M., 2016. Multi-decadal trends in global terrestrial evapotranspiration and its

- 712 components. *Scientific Reports* 6. doi:10.1038/srep19124.
- 713 Zhou, S., Williams, A.P., Lintner, B.R., Berg, A.M., Zhang, Y., Keenan, T.F., Cook, B.I., Hagemann, S., Seneviratne,  
714 S.I., Gentine, P., 2021. Soil moisture–atmosphere feedbacks mitigate declining water availability in drylands.  
715 *Nature Climate Change* 11, 38–44. doi:10.1038/s41558-020-00945-z.
- 716 Zhu, G., Li, X., Zhang, K., Ding, Z., Han, T., Ma, J., Huang, C., He, J., Ma, T., 2016. Multi-model ensemble prediction  
717 of terrestrial evapotranspiration across north China using Bayesian model averaging. *Hydrological Processes* 30,  
718 2861–2879. doi:10.1002/hyp.10832.
- 719 Zhu, G., Zhang, K., Chen, H., Wang, Y., Su, Y., Zhang, Y., Ma, J., 2019. Development and evaluation of a simple  
720 hydrologically based model for terrestrial evapotranspiration simulations. *Journal of Hydrology* 577, 123928.  
721 doi:10.1016/j.jhydrol.2019.123928.

## Highlights

### **Improvement of evapotranspiration simulation in a physically based ecohydrological model for the groundwater-soil-plant-atmosphere continuum**

Kun Zhang, Gaofeng Zhu, Ning Ma, Huijing Chen, Shasha Shang

- A newly modified eco-hydrological model was proposed to estimate terrestrial ET.
- SiTHv2 improved ET estimates by 27% over the prior version validated at 175 flux stations.
- SiTHv2 ranks well among the popular global terrestrial ET algorithms.

**CRediT authorship contribution statement**

**Kun Zhang:** Conceptualization, Methodology, Writing – original draft, Formal analysis, Funding acquisition. **Gaofeng Zhu:** Conceptualization, Writing – review & editing, Funding acquisition. **Ning Ma:** Writing – review & editing, Data curation. **Huiling Chen:** Methodology, Figure plotting. **Shasha Shang:** Writing – review & editing.

**Declaration of Competing Interest**

The authors declare that they have no known competing financial interests or personal relationships that could have appeared to influence the work reported in this paper.